Author's preprint of final accepted version.
Final TWS version available at https://doi.org/10.1016/j.tws.2019.03.043

FE Simulation of Ceiling Deployment of a Large-Scale Inflatable Structure for Tunnel Sealing

Iole Pecora, Eduardo M. Sosa[1], Gregory J. Thompson, and Ever J. Barbero

Department of Mechanical and Aerospace Engineering

West Virginia University, Morgantown, WV 26506-6106, USA

[1] Corresponding Author. E-mail: eduardo.sosa@mail.wvu.edu

Abstract

Transportation tunnels such as railway or subway tunnels in large metropolitan areas have been identified as particularly vulnerable to different threats such as propagation of toxic gases, smoke originated by human activities, or flooding originated by climatic events such as hurricanes and severe weather. The implementation of large-scale inflatable structures to plug specific locations of the tunnel system to minimize the consequences of the propagation of disastrous events is now possible. However, even with the successful results obtained in experimental evaluations, the development of simulations that can predict the performance of the inflatable in advance to reduce the number of experimental iterations is still essential. The finite element simulations presented in this work are focused on reproducing deflation, folding, and placement procedures followed by the simulation of deployment and inflation of a large-scale inflatable from the ceiling of a tunnel segment. Simulation results show that a very compact shape can be achieved by implementing a controlled deflation and a combination of translational and rotational planes to reach the final folded shape. Moreover, the implementation of passive restrainers to control the movement and release of the membrane during different stages of the deployment contributed to reach higher levels of local conformity of the inflatable to the tunnel perimeter, which also translated in a better sealing capacity of the inflatable to the tunnel profile by approximately 16% increase in the contact surface area.

Keywords: Abaqus, Ceiling, Deflation, Deployment, Finite Element Simulation, Folding, Inflation, Membrane, Tunnel, Inflatable Structure.

1. Introduction

The safety of transportation tunnels has become a great concern for transportation and government entities in the last decade [1-3]. Transportation tunnels have been identified as particularly vulnerable to different threats originated by human activities or extreme climatic events. Flooding of tunnels have been particularly severe and produced significant damage to transportation tunnel systems of Chicago in 1992 [4] and New York City during Hurricane Sandy in 2012 [5]. Finding solutions to minimize the consequences of disastrous events has become critical to increasing the resiliency of transportation subway tunnel systems. One possible solution to contain the propagation of gases or flooding is the implementation of large-scale inflatable structures at specific locations of the tunnel system. When a threat happens, a sensing system detects it and triggers the activation of an inflation system which can deploy, inflate and pressurize the inflatable structure in a few minutes [6-7]. When the inflatable structure is completely inflated, it acts as a barrier, held mostly by friction, and isolates the compromised region to contain the threat. The feasibility of this concept was tested in a full-scale setup using an inflatable manufactured from a single-layer fabric material, folded, installed in a service tunnel, deployed from the ceiling of the tunnel and then fully inflated with air at relatively low pressure (less than 7 kPa gauge or 1 psi gauge) in approximately three minutes as reported in Martinez et al. [8]. After the demonstration of feasibility, and in the last few years, extensive experimental evaluations were conducted to evaluate and understand key aspects of the operation and mechanical behavior of large-scale inflatable structures as reported in [9-12].

From the operational point of view, experimental results showed that the implementation of a large-scale inflatable for sealing one or more segments of a tunnel system is divided into three main phases. Preparation, folding and installation of the inflatable occur during Phase 1; in this phase, the inflatable structure is folded and placed within a portable container that is then transported to a specific location of the tunnel segment and pre-installed on duct banks or the ceiling of the tunnel. Phase 2 starts when a sensing system detects a threatening event which triggers the initial deployment and inflation at a low pressure of the inflatable. Once the inflatable is in position, Phase 3 continues with the pressurization of the inflatable structure to keep it in place to provide the required frictional resistance to contain the propagation of flooding or propagation of gases or smoke [12]. Considering these phases, the main objective of this work is to create Finite Element (FE) models able to simulate the procedures for the preparation (Phase 1) and deployment and inflation (Phase 2) of the single layer inflatable used in the tests reported by Martinez et al. [8]. Experiments at full scale demonstrated that there is minimal change in the inflatable geometry during Phase 3 and that the sealing effectiveness of the inflatable system is significantly affected by how the inflatable is prepared during the folding and installation process and how it positions during the initial stages of deployment [12]. Using the techniques presented by Sosa et al. [13-14] as a starting point, this work introduces new ways to improve control of the membrane of the inflatable since it plays an important role on the final global and local conformity of the inflatable to the tunnel. This work also aims to demonstrate that using a simplified geometry for the inflatable it is possible to achieve similar or higher levels of local conformity as those obtained using a fitted shape of the inflatable adopted by Martinez et al. [8]. In particular, the FE models presented in this work were developed to simulate the following operations:

- Folding methods that follow the procedures implemented experimentally, including the implementation of a controlled deflation to reach a generally flat shape and the implementation of a folding procedure for the flat shape that minimizes the storage volume.
- Initial deployment and inflation, which required the definition of placement procedures of the folded shape in the storage area of the tunnel cross-section, the design of an inflator system taking into account the available experimental results, and the definition of a sequence of deployment and inflation under confined conditions.

2. Model Generation

2.1 Modeling Tools

The Simulia Finite Element simulation package was implemented in this work. In particular, the geometry and meshing of the model were generated using Abaqus/CAE [15]. All the nodes and the element were later renumbered with HyperMesh tools [16], and the model properties were compiled in an Abaqus input file (.inp) that also included material, mechanical and thermodynamic properties needed for the definition of the different stages of the models. All the models were solved with the explicit solver available in Abaqus/Explicit. Abaqus/Viewer was used for the visualization and post-processing of the simulation results.

2.2 Geometries

The two main components of the model are the inflatable structure and the tunnel segment representative of the confined environment in which the inflatable will be installed and inflated. Additional components included a rigid surface called the "base" representative of the floor where the folding procedures take place as well as folding planes used to simulate the folding procedures implemented experimentally.

The inflatable structure modeled in this work consists of a cylinder with two spherical end caps. The radius of the cylinder is 2.794 meters, its length is 3.657 meters, and the radius of the spherical end caps is 3.658 meters each. The model of the inflatable follows the dimensions and material properties of the full-scale prototype used in the experiments reported in [8]. The perimeter of the cylindrical portion of the inflatable was designed to include an 11% oversizing with respect to the nominal tunnel perimeter to account for possible bridging of the membrane around the corners as well as the presence of other elements that could interfere with the local conformity of the inflatable around the tunnel perimeter. Figure 1(a) shows a plan view the overall shape and dimensions of the inflatable structure and Figure 1(b) shows the cross-section of the tunnel segment in which the folded inflatable structure will be positioned and inflated.

The generation of the FE model of the inflatable structure was completed during the pre-processing in which the geometry of the model, material properties, element type, and contact interaction properties were defined. The initial geometry of the inflatable structure was created using a three-dimensional deformable shell through Abaqus/CAE. The shell surface was then partitioned in several auxiliary surfaces as shown in Figure 2. The partitions on the cylindrical part of the inflatable structure were created to define folding surfaces and folding lines that were used as reference lines at the different stages of the simulation. Additional surface partitions were created on the spherical end caps to have a more uniform mesh. The FE model of the tunnel, base and folding planes were created via three-dimensional rigid shell surfaces generated in Abaqus/CAE. Since these surfaces are considered non-deformable, they were meshed using linear quadrilateral rigid elements R3D4 [15]. The meshes of the tunnel, base, and folding planes are shown in Figure 3.

2.3 Membrane Material

The membrane of the inflatable structure is a single layer coated fabric with a thickness t = 0.00078 meters and a density of ρ = 1346 kg/m^3. The models built in this work implement the mechanical properties of Ferrari Precontraint 1002 [17, 18] which was the material used for manufacturing the full-scale prototype tested by Martinez et al. [8]. The fabric of the inflatable used in the experiments was modeled using M3D3 membrane elements [15]. The fabric material is assumed to behave as an orthotropic fabric with approximately equal tensile strengths in the warp and fill directions ($\sigma_{max} = 1.026 \cdot 10^8$ Pa or $\sigma_{max} \times t$ = 80 kN/m). The fabric also includes shear strength adapted from the experimental results reported in [19]. The constitutive relationship under tensile load for the fill and warp direction of the fabric material is illustrated in Figure 4(a) and the constitutive relationship under shear loads is illustrated in Figure 4(b). These two curves were introduced in the model generation in a tabular form.

Although the actual fabric material does not have stiffness under compression, the stability and the convergence of the FE models using an explicit solver such as Abaqus/Explicit required the definition of an artificial compressive strength in order to prevent excessive distortions or the collapse of membrane elements. The inclusion of an artificial compressive strength as a small percentage of the tensile strength is commonly used in the simulation of automobile airbags [15]. For the models created in this work, different compressive strengths in the range of 0.01% to 1% of the maximum tensile strength were assigned to the constitutive model according to the type of simulation process being performed: deflation, folding or inflation.

3. Unconfined Inflation and Pressurization

3.1 Stress Evaluation and Mesh Convergence Study

Three different mesh densities were generated to evaluate the membrane stresses of the inflatable structure under unconfined pressurization conditions. The nominal shape illustrated in Figure 2 was modeled with 27528, 48948 and 95902 elements and these meshes were identified as Mesh A, Mesh B, and Mesh C, respectively. A quasi-static analysis using Abaqus/Explicit was implemented to pressurize the inflatable structure starting from the nominal shape shown in Figure 2 representative of the unconfined pressurization. This shape was uniformly pressurized following a ramp function for 10 seconds until the internal pressure reached a maximum value of P = $6.895 \cdot 10^3$ Pa (~1 psig). The internal pressure P corresponds to the value of the internal (or gauge) pressure measured during the experiments reported in [8]. During the simulations of pressurization, the gravity load was active and followed the same ramp function of the internal pressure and was active. No mass scaling or damping was used in the convergence analysis. The circumferential or hoop stress σ_1 and the longitudinal stress σ_2 on the cylindrical portion and on the spherical end caps were evaluated first analytically and then numerically in order to estimate the FE models accuracy for different mesh densities. The analytical values corresponding to (σ_1) and (σ_2) for cylindrical and spherical end caps were evaluated using classical equations for thin-walled structures under internal pressure as follows:

$$S_{11} = \sigma_{1_{Cylinder}} = \frac{PR_{Cylinder}}{t} = 24.71 \cdot 10^6 \text{ Pa} \qquad \text{Eq. (1)}$$

$$S_{22} = \sigma_{2_{Cylinder}} = \frac{PR_{Cylinder}}{2t} = 12.35 \cdot 10^6 \text{ Pa} \qquad \text{Eq. (2)}$$

$$\sigma_{1_{cap}} = \sigma_{2_{cap}} = \sigma = \frac{PR_{cap}}{2t} = 16.17 \cdot 10^6 \text{ Pa} \qquad \text{Eq. (3)}$$

Where the internal pressure is $P = 6.895 \cdot 10^3$ Pa, the membrane thickness is $t = 0.00078$ m, the radius of the cylindrical region is $R_{Cylinder} = 2.795$ meters and the radius of the spherical end cap is equal to $R_{cap} = 3.658$ meters. For the evaluation of the mesh convergence, the hoop stress (S_{11}) in the cylindrical region was chosen as a control parameter. Contours of stress distributions in the hoop directions related to the three mesh densities are shown in Figure 5. Four nodes around the middle cross-section of the cylinder region were chosen to evaluate the average of the hoop stresses. The average values obtained from the simulations are summarized in Table 1 and compared to the analytical value provided in Eq. (1). Results summarized in Table 1 show that the difference between the stress value of the analytical solution and the values predicted by the simulations is negligible indicating that any of the proposed meshes would predict the stresses with acceptable accuracy. Although it is recognized that a more dense mesh is more expensive in terms of computing time, the implementation of folding procedures required a relatively refined mesh to minimize the volume of the final folded shape and at the same time prevent inter-element penetrations and intersections. Therefore, Mesh C was adopted in the models described in the following sections.

The selection of a more dense mesh comprised of smaller elements also contributed to minimizing inter-element intersection and penetrations which are undesired effects feasible to appear in large deformation analyses involving membrane elements [15-16]. In the simulation of folding, initial deployment and inflation, different parts of the inflatable structure can come into contact with itself and with other parts of the model. In order to avoid inter-element penetrations and intersections as well as fictitious structural penetrations, it was necessary to define contact interactions and contact controls [15]. In the simulations carried out in this work, contact interactions were defined between the inflatable structure and the auxiliary components such as the base, the folding planes and the inner surface of the tunnel segment, and also between the inflatable structure and itself. In all the simulations, a static friction coefficient of $\mu = 0.20$ was used for the fabric-to-fabric friction. In the simulations of controlled deflation and folding, a static friction coefficient of $\mu = 0.5$ was adopted between the deflating or deflated structure and the base and folding planes to avoid sliding of the membrane during the folding steps. For the simulation of initial deployment and inflation within the tunnel segment, a friction coefficient of $\mu = 0.4$ was defined between the membrane of the inflatable and the inner tunnel surface. These values are based on experimental evaluations at the coupon level reported in [17] and are in the same range of the values used in previous simulations reported in [13-14].

3.2 Mass Scaling: Initial Evaluation

The implementation of relatively dense meshes along with an explicit solver to simulate inflation and controlled deflation as quasi-static problems can result in very long computing times. One way to reduce that computing time is by implementing mass scaling. Mass scaling is a common technique implemented to reduce the simulation time by increasing the stable time increment Δt. The implementation of the mass scale factor produces a decrease of the computing time and, depending on the type of structure and loading pattern, may produce an increase of inertial effects [15, 23]. The implementation of mass scaling is convenient in solving quasi-static problems, where the mass is not subject to significant changes in its kinetic energy. However, it must be used carefully to ensure that the inertial effects do not dominate and change the solution [15]. There is not an exact way to find an appropriate value of the mass scaling factor as it depends on the characteristics of the problem being solved. For this reason, four fixed values of the mass scaling factor (MSF = 1, 10, 100, 1000) were evaluated to determine an initial value to implement in the subsequent simulations presented in this work. The evaluation of different MSF was carried out to determine a value for the MSF that was sufficiently large to reduce the computing time of the simulations but at the same time, not too large to induce inertial effects that are not present in the behavior of the actual structure being simulated. The unconfined inflation was used as a benchmark case for the initial MSF evaluations. The MSFs were applied to the model of the inflatable from the beginning of the simulation and maintained constant until the completion of the simulation. The inflation started with the membrane structure resting deflated on the rigid base shown in Figure 3(b). A constant air mass flow rate of $\dot{m}$ = 0.48 kg/sec was applied for 276 seconds. At this rate, the internal pressure reached a value of about P = 6.895·103 Pa at the end of the inflation. No damping was included in the evaluation of the different MSFs. The gravity load was active during the entire simulation of unconfined inflation. As noted in [15, Section 11.7.1], in simulations with Abaqus/Explicit, gravity loads are not affected by mass scaling as the density associated with the gravity load vector remains unscaled.

The first indicator used to evaluate the influence of the MSF was the total computational time required to complete the simulation of the unconfined inflation. The evaluation was performed using the same computer utilizing a single processor for each value of the MSF. Each case was run separately to avoid interference during the computation of the solution. The computing times corresponding to each MSF are summarized in Table 2. Results show that the simulation with an MSF = 1 took about 456 hours (about 19 days), which is an excessively long time. The reason for such a long computational time is that the mesh of the deflated shape includes several small and poorly shaped elements that control the smallest characteristic length L_e of the mesh. Since stable time increment is determined by $\Delta t = L_e / c_d$, where c_d is the dilatational wave speed of the material defined as $c_d = \sqrt{E/\rho}$, where E is the elastic modulus and ρ is the material density. If the material density is increased artificially by a factor f^2, the wave speed increases by a factor of f and the stable increment increases by a factor f, as well [15], and therefore reduces the total computational time. So, an increase of MSF from 10 to 100 to 1000 produced a significant decrease of the computational time from 83 hours to 46 to 19 hours, respectively. But, as anticipated, increasing values of MSFs also produced an increase of inertial effects, particularly for a MSF = 1000.

The second indicator used for analyzing the influence of the MSFs was the kinetic energy (KE) to internal energy (IE) ratio (KE/IE). It is common to consider the behavior of a structure as quasi-static if the KE/IE ratio is typically below 5% to 10% [15]. Results shown in Figure 6(a) indicate that for the MSFs 1, 10 and 100, the amplitude of the KE/IE ratio is nearly zero for 93% of the duration of the inflation process. The peak KE/IE ratio is reached at the end of the inflation when the inflatable is fully inflated, and the self-weight counteracts the inflation pressure producing some vertical bouncing that dissipates as the inflator is deactivated and the inflatable reaches a position of equilibrium. The bouncing effect is significant for MSF = 1000, where the KE/IE reaches a peak of 0.2896, and less significant for the MSF = 100 and MSF = 10, where the peak energy ratios were 0.0736 and 0.0075, respectively. The simulation results obtained from the implementation of different values of MSF indicate that an MSF = 100 is large enough to reduce the computing time to a relatively reasonable value (46 hours), but at the same time, it is not too large to induce inertial effects that would increase the energy ratio above the threshold of 10% for the process to be considered quasi-static. Therefore, a value of MSF = 100 was initially adopted for the subsequent models presented in this work. Additional verification of the influence of the MSFs was made for the confined inflation cases presented in the next sections, and the results are summarized in Section 5.6.

3.3 Damping

The simulation of unconfined inflation presented in Section 3.2 was also used to initially evaluate the inclusion damping in the models. The presence of viscous damping was added to the simulations by using a mass-proportional Rayleigh damping factor α. Six different values of α (0.0, 0.2, 0.4, 0.6, 0.8, and 1.0, all in units of s^{-1}) were analyzed maintaining the stiffness-proportional factor β constant and equal to $1 \cdot 10^{-6}$ as the membrane has no stiffness for practically the entire duration of the inflation. In the evaluations of the different damping factors, the mass scale factor was set to 100. In order to understand the impact of increasing values of α, the kinetic to internal energy (KE/IE) ratio was also used as a control output.

Results shown in Figure 6(b) indicate that the amplitude, frequency of oscillations and peaks of the KE/IE ratio decreased as the magnitude of α increased. Results show that an increase of the mass-proportional Rayleigh damping produces a decay in amplitude of high-frequency oscillations of the KE/IE ratio. Not including damping (α = 0) in the model produced local oscillations associated with membrane trembling manifested by large oscillations of the KE. On the other hand, for values of α in the range of 0.6 to 1.0, the dampening effect is significant as there are practically no local or major global oscillations as the membrane inflates resembling the inflation of the membrane in an increasingly viscous surrounding media. This behavior is considered not realistic and therefore maintaining α in the range between 0.2 and 0.4 seemed to reproduce a more realistic behavior of the membrane as the unconfined inflation was completed. An initial value of $\alpha = 0.2$ was adopted for the remaining simulations presented in the next sections. In Figure 6(b) it is also worth to note the quasi-static nature of the unconfined inflation in which the KE/IE ratio for the different values of α remained close to half a percent for about three quarters of the inflation process and reached peaks in the range of 3.5 to 6% at the end of the inflation. This may not be the case of the initial deployment and confined inflation, so an additional verification of the influence of the mass-proportional damping factor α is presented in Section 5.6.

4. Controlled Deflation, Folding, Placement and Confined Inflation

4.1 Controlled Deflation (Case 0)

The purpose of the simulation of a controlled deflation is to reproduce experimental procedures implemented for folding a large-scale inflatable. The objective of the controlled deflation is to reach the flattest possible shape with the minimum amount of wrinkles on the flattened membrane to minimize the volume of the final folded shape and ensure subsequent tunnel surface conformability during confined inflation. The simulation started with the nominal shape of the inflatable structure illustrated in Figure 2, with a mesh density corresponding to Mesh C, and subject to an internal uniform pressure equal to the gravity pressure (P_g = 10.3 Pa) to balance the external load due to the application of the gravity load. Modeling of the internal pressure required the definition of a cavity inside the inflatable representative of the internal volume being filled. The internal uniform pressure was imposed as a boundary condition to the cavity reference node (degree of freedom 8 [15]). Since the formation of large wrinkles depends on how fast the internal uniform pressure is reduced, the controlled deflation followed a decreasing ramp function with a shallow slope of 0.000025 Pa/second. At this deflation rate, the simulation of the deflation was considered a quasi-static problem. The very slow deflation rate also prevented the sudden collapse of the membrane during the deflation which minimized the change in kinetic energy and according to the D'Alambert's principle [24], it minimized the inertial effects too. Although the controlled deflation was performed in one simulation step, the simulation was stopped every four time-increments to have better control of the deflation of the membrane. At each interruption, the coordinates of the resultant shape were exported first to Abaqus/CAE and then to Hypermesh to inspect the mesh and detect if the membrane elements were affected by inter-element penetrations and intersections, and in such case, correct them before continuing with the simulation. This process was designated as the "cleaning process," after which, the controlled deflation with the corrected mesh continued using the same initial conditions of pressure ($P_{int} = P_g$) with the same decreasing ramp function. The sequence of the controlled deflation is shown in Figure 7.

4.2 Folding and Placement

The flattened shape of the inflatable obtained at the end of the controlled deflation technique was the starting point of the folding sequence. It included the definition of two rotating planes (FP1, FP2) and two translational planes (FP3, FP4) as shown in Figure 8(a). The partial folds of the membrane of the inflatable were created by imposing rotational (φ_x= U4, φ_y= U5, φ_z= U6) and translational (u_x= U1, u_y= U2, u_z= U3) boundary conditions to the reference nodes of the folding planes as illustrated in the sequence of Figure 8(b) to 8(f). The folded shape obtained at the end of the folding sequence (Figure 8(f)) was placed inside the tunnel segment as illustrated in the sequence of images of Figure 9. The placement process began with the folded shape pre-positioned at the center of the tunnel, as illustrated in Figure 9(a) and continued by imposing rotational and translational boundary conditions to the reference node of the folded shape defined as a rigid body as illustrated in the sequence of Figure 9(b) to 9(e). Once the folded shape was positioned on the ceiling of the tunnel, it was connected to the ceiling of the tunnel using three lines of nodes defined along the cylindrical portion of the inflatable as illustrated in Figure 10. The displacements of the nodes in the attaching lines were restricted in all three directions. Only rotations were allowed in these nodes. These boundary conditions represented the ties that fastened and restrained the inflatable structure to the ceiling of the tunnel in the experiments reported by Martinez et al. [8].

4.3 Inflator Design for Confined Inflation

The Uniform Pressure Method [15] was used to define an inflator that can be run in Abaqus/Explicit. This inflator required the definition of a gas mass flow rate and a gas temperature as a function of the inflation time. The gas used to fill the volume of the inflatable structure was atmospheric air at sea level. The air temperature was kept constant and equal to the ambient temperature (T = 228.15° K or 15° C). Additional thermodynamic properties [20] corresponding to air, as well as the coefficients of the Shomate equation [21] needed for the definition of the inflator, are summarized in Table 3 and Table 4.

The nominal unconfined volume of the inflatable structure according to the dimensions shown in Figure 1 is V_0 = 116 m^3. However, considering the oversizing of the inflatable as well as the dimensions of the tunnel section, a more detailed estimation of the internal volume adopted for the confined inflation included two parts. The first one includes the cylindrical portion evaluated taking into account the volume of a segment of the tunnel with a circular cross-section with a radius of 2.51 meters and a length equal to the same length of the nominal cylindrical portion of the inflatable and equal to 3.66 meters. The second part considers the nominal volume of the spherical end caps, plus an increment of the volume due to the stretching of the membrane produced by the internal target pressure of $P = 6.895 \cdot 10^3$ Pa (~1 psig) expected to be reached at the end of the inflation as reported in [8], produced a confined inflation volume of V_c = 108.2 m^3. An initial estimation of the air mass flow rate can be obtained from:

$$\dot{m} = \dot{V}\rho \qquad \text{Eq. (4)}$$

Where, $\dot{V}$ is the volume rate and ρ is the density of air. Although in the experiments reported in [8] the original target was to deploy and inflate in about three minutes, the actual inflation took 4:36 minutes (276 seconds) due to "flow loses in the in the hose and because the fan was not running at its maximum speed" as indicated in [8]. With this consideration, and taking the confined volume V_c and the total inflation time t = 276 seconds, the volumetric flow rate is given by:

$$\dot{V} = \frac{108.2}{276} = 0.392\ \frac{m^3}{sec} \qquad \text{Eq. (5)}$$

Substituting the numerical values into Eq. (4), the density of air indicated in Table 2, the air mass flow rate for confined inflation is:

$$\dot{m} = 0.392 \times 1.225 = 0.480\,\frac{kg}{sec} \qquad \text{Eq. (6)}$$

This air mass flow rate $\dot{m}$ was used for confined inflation in the remainder simulations described in the following sections.

4.4 Initial Deployment and Inflation (Case 0)

The sequence of initial deployment and inflation started with the folded shape positioned in the storage area on the ceiling of the tunnel as shown in Figure 10. The tunnel segment was assumed to be a rigid body fixed in the X, Y, and Z global directions. The simulation was performed in one step in which gravity and the inflator were activated sequentially. Gravity was applied as an impulse at the beginning of the simulation, and the inflator was activated with 2 seconds of delay to reproduce experimental results [8]. During the deployment and inflation of folded membrane, it was necessary to call the reference mesh created based on the nominal shape shown in Figure 2 so that it was able to restitute the membrane to the unstressed condition existing before the controlled deflation and the folding process. Referencing the folded mesh to a reference mesh is a common procedure in the simulation of automobile airbags [15, 24-27]. The entire initial deployment and inflation sequence were set to take place in 276 seconds plus four additional seconds for inflator deactivation and pressure stabilization for a total simulation time of 280 seconds.

Figure 11 shows a sequence of images captured from the simulation results compared to a sequence of images captured during the experiments [8]. Results show that even though the simulation generally followed the sequence seen in the experiment, the apparent flexibility of the membrane material in the simulations did not replicate the behavior observed in the experiment. From the sequence shown in Figure 11(a), the membrane seems to have less flexibility than the flexibility observed in the actual prototype. This behavior is attributed to the artificial compressive strength adopted in the definition of the membrane material. In the model of Figure 11, the compressive strength was initially assumed to be σ_{CS6} = 0.5% of the maximum membrane tensile strength for a strain $\varepsilon = -0.014$. A parametric evaluation with decreasing values of σ_{CS} was carried out and the results are described in Section 4.5.

On the other hand, considering the global conformity of the inflatable to the tunnel, the fully inflated shape at the end of the simulation was similar to the shape observed in the experiments as shown in Figure 11. However, considering the local conformity, the simulations showed that the inflatable was not able to conform to at least two corners of the tunnel profile, as shown in Figure 11 the images corresponding to the end the inflation. In this regard, a detailed view of the lack of local conformity is illustrated in Figure 12, which shows two clear contact gaps in the right corners of the tunnel profile. The formation of the gaps is attributed to the lack of uniform distribution of the membrane material which accumulated on the tunnel floor. It is speculated that the combination of the reduced membrane flexibility noted previously, the lack of control of the membrane once it was deployed by gravity, as well as the friction between the membrane and the tunnel floor opposed the action of the inflation pressure. This combination of factors did not allow full expansion of the membrane, so it was not able to be transferred to the lateral portions of the tunnel and therefore producing the contact gaps illustrated in Figure 12(b).

Time histories of internal pressure (PCAV), volume (CVOL) along with the inflator step function with a constant mass flow rate of $\dot{m}$ = 0.48 kg/sec are plotted in Figure 13. This plot is divided in three main regions: I. Deployment of the inflatable by the action of gravity from t = 0 to t = 2 seconds; II. Inflation in which there is a nearly linear increase of the volume of the inflatable as the air mass accumulates from t = 2 seconds to t = ~250 seconds, while the gauge pressure remains close to zero; III. Pressurization from t = ~250 seconds to t = 276 seconds, in which the inflatable cannot expand any further and any additional air flow going into the inflatable compresses producing a raise in the internal pressure until the inflator is deactivated at t = 276 seconds. Results on Figure 13 show that the inflator produced at the end of the inflation values of the gauge pressure and internal volume close to the target values. The gauge pressure reached a value of $6.606 \cdot 10^3 Pa$ which is 4.3% lower than the target value of $6.895 \cdot 10^3 Pa$. The internal volume reached a value of $103.325\ m^3$, which is 4.6% lower than the initially estimated value of V_c. The small difference in the volume is attributed to the lack of local conformity caused by the inability of the membrane to conform to the corners of the tunnel profile as noted previously.

4.5 Influence of Stiffness of the Membrane

One of the challenges of the simulation of folding and unrolling or deployment of fabric materials with membrane elements is that the folding process can produce excessive distortion due to compression of a few or several elements along, for example, folding lines. The excessive distortion of elements can negatively affect the stability of the solution and convergence of the explicit solver by reducing the order of magnitude of the stable time increment Δt [15]. One way to minimize the effect of excessive distortion is to assign an artificial compressive strength to the constitutive model corresponding to the fabric material. This artificial compressive is typically a very small percentage of the actual tensile strength of the fabric material, and its magnitude is adjusted to avoid excessive artificial stiffening of the membrane during the simulations. With these considerations, a parametric study was conducted changing the value of the artificial compressive strength included in the definition of the constitutive model of the fabric material shown in Figure 4(a). For the different values of the compressive strength, the deformation was kept constant at a value of $\varepsilon = -0.014$, which is in the same order of magnitude of the deformation in tension for the target pressure of $P = 6.895 \cdot 10^3$ Pa. Six values of compressive strength σ_{CS} were evaluated. Values ranged between 10,000 Pa to 500,000 Pa which are the range of ~0.01% to ~0.5% of the fabric tensile strength of $\sigma_{max} = 1.026 \cdot 10^8$ Pa. The change in the ratio between the artificial compressive strength and the deformation produced a change in the apparent flexibility of the membrane. The objective of trying different ratios was also to better reproduce in the simulations the membrane behavior observed in the experiments reported in [8].

To quantify the influence on the membrane flexibility produced by different values of the artificial stiffness in compression, the strain energy (SE) was used as output for evaluation of the simulation results. Figure 14 compiles the strain energies computed for different values of the artificial compressive strength. The data in Figure 14 shows that the SE developed during the initial falling and unfolding of the membrane (from t = ~1 to t = ~10 seconds) decreased as the artificial compressive strength decreased, meaning that the membrane material displayed a more flexible behavior. Figures 11 shows a comparison of the experimental test with the simulations of the initial deployment and inflation corresponding to $\sigma_{(CS1)}$ (~0.01% of σ_{max}), $\sigma_{(CS3)}$ (~0.05% of σ_{max}) and $\sigma_{(CS6)}$ (~0.5% of σ_{max}) selected as representative cases. Simulation results shown in Figure 11 indicate that, as expected, a decreasing compressive strength produced a more flexible behavior of the membrane during the initial unfolding and subsequent inflation. From Figure 11, it is concluded that a value of artificial compressive strength of 10,000 Pa ($\sigma_{(CS1)} \sim 0.01\%\ \sigma_{max}$) reproduced a membrane behavior that was closer to the membrane behavior seen in the experiments and therefore, was adopted in the subsequent simulations presented in the following sections.

5. Confined Inflation – Controlled Membrane Release

Based on the results corresponding to Case 0, an enhanced technique was developed to improve the lack of local conformity seen at the end of the inflation. This enhanced technique included not only the controlled deflation described previously but also the implementation of additional displacement boundary conditions to specific folding lines and portions of the membrane. These additional displacement boundary conditions were imposed to create initial pre-folds incorporated into the inflatable to prevent the formation of major wrinkles as well as to improve the membrane distribution over the deflated shape. The addition of pre-folds is also complemented with the addition of passive restrainers (also known as tie-downs or break lines [12-13]) incorporated with the purpose of keeping the initial folds in place while the remaining folding operations are completed, and also for holding of the membrane during the initial deployment and subsequent controlled release near the end of the inflation process.

5.1 Controlled Deflation Including Pre-folding Steps

Two cases of controlled deflation including pre-folds were simulated: the first one, Case A, included only one pre-fold, and the second one, Case B, included two pre-folds. Case A was developed to simulate the technique of the controlled release of the membrane similar to the one implemented in the experiment and previous simulations [8, 12-14]. Case B was also created to show the potential of this enhanced technique and to emphasize the possibility of achieving a higher level of local conformity of the membrane when required to conform into more intricate tunnel profiles that might include several corners or geometric changes that make the local conformity more challenging. In the cases presented next, the position of the initial pre-folds was dictated by the position of folding surfaces of the membrane that did not conform to specific locations (corners) in the tunnel profile at the end of the inflation as shown in Figure 12.

5.1.1 Case A

As in Case 0, the initial shape used at the beginning of the simulation was the initial nominal shape of the inflatable structure shown in Figure 2. The position of the initial single pre-fold was defined based on the position of the folding surfaces (colored bands in Figure 2) necessary to cover the right side corners of the tunnel profile (see Figure 1(b)). In order to achieve a symmetric flat deflated shape, a second auxiliary pre-fold was created on the opposite side of the first pre-fold with the purpose of obtaining an equal distribution of the membrane material as shown in Figure 15. In conjunction with the controlled deflation, translational boundary conditions were applied to the reference lines to guide the formation of the pre-folds as illustrated in the sequence of images of Figure 16. Once the two initial pre-folds were formed, as illustrated in Figure 16(e), equally spaced nodes located at the bottom line (BL) and the top line (TL) were linked with connector elements to maintain these lines close to each other. Linking these lines contributed to maintain the shape of the pre-fold for the rest of the controlled deflation. At the end of the controlled deflation, an additional vacuum pressure of $P_v = 700$ Pa was applied to reach an even flatter folded shape, as illustrated in Figure 16(i).

5.1.2 Case B

Case B included the two pre-folds created in Case A, plus a third pre-fold. The controlled deflation of Case B started with the shape illustrated in Figure 16(d). The position of the third pre-fold is shown in Figure 17 and corresponds to the position of the lower right corner of the tunnel profile. As in Case A, in addition to continuing the controlled deflation, translational boundary conditions were applied to the top (TL) and bottom (BL) lines to guide the formation of the third pre-fold, as illustrated in the sequence of images of Figure 18. Once the formation of the third pre-fold shown in Figure 18(c) was completed, equally spaced nodes located along the top (TL) and bottom (BL) lines of the fold were linked with connector elements to maintain the lines close to each other during the remaining folding steps. As in Case A, a vacuum pressure of P_v = 700 Pa was applied in the last stage of the controlled deflation to obtain a flatter folded shape as illustrated in Figure 18(d).

5.2 Cases A and B: Folding and Placement

As in Case 0, the flattened shapes obtained for Cases A and B were folded imposing translational and rotational boundary conditions to the folding planes FP1 and FP2 illustrated in Figure 19. The folding procedure was the same for both cases. Selected nodes on the top and the bottom edges of each pre-folding lines were temporarily restrained using connector elements to avoid sliding of the membrane material during the folding process and to prevent distortion of the pre-folds. Once the folding was completed, the final folded shapes were placed on the ceiling of the tunnel as described in Section 4.2. Figure 20 compares two folded shapes positioned on the ceiling of the tunnel. The folded shape corresponding to Case 0 is illustrated in Figure 20(a), whereas Figure 20(b) shows the folded shape obtained using the pre-folds (Cases A and B). These two images show that in the longitudinal and transversal profiles there is a significant reduction of the overall folded volume and a more uniform distribution of the membrane material along the longitudinal direction of the tunnel. For Case 0, the overall folded thickness at the tunnel center line was $w_0 = 0.32\ m$, while for Cases A and B, the overall thickness was $w_{A-B} = 0.18\ m$, which is nearly half of Case 0, and within the limit of w = 0.20 m available for storage of the folded prototype tested in the full-scale experiments [8].

5.3 Design of Passive Restrainers

One of the key aspects for achieving high levels of local conformity of the membrane around the intricacies of a tunnel profile is by controlling the release of the membrane during the later stages of the inflation and beginning of the pressurization (see zones delimited in the pressure time history plotted in Figure 13). This technique was implemented in the experiments reported in [8] as well as in the experiments reported in [10] and [12]. The time history of internal pressure obtained from the simulation of confined inflation without control of the membrane (Case 0, Figure 13) provided an initial estimation of the value of the gauge pressure at the onset of the beginning of the pressurization phase. At $t \approx 250$ seconds, the pressure was equal to $P_R \approx 180$ Pa. This value of inflation pressure P_R is the pressure at which the passive restrainers simulated with uniaxial connector elements will have to break to release the membrane stored in the pre-folds. Equating P_R to P_{conn} allows obtaining an initial estimation of the magnitude of the force that each passive restrainer will have to take before breaking. The passive restrainers are placed joining folding lines (TL and BL shown in Figures 15 and 17), which are located along the cylindrical portion of the inflatable. The hoop stress on the cylindrical portion of the inflatable right before reaching contact with the inner surface of the tunnel can be estimated as:

$$\sigma_{hoop} \times \mathrm{t} = P_{conn}\, R = 451.8\ \frac{N}{m} \qquad \text{Eq. (7)}$$

Where t is the thickness of the membrane, $P_{conn} = P_R = 180$ Pa is the pressure necessary to break the passive restrainers, and $R \approx 2.51$ meters is the radius of the cross-section of the cylindrical of the inflatable structure at $t = 250$ seconds. The value of R is initially assumed to be equal to the nominal radius of the tunnel $R = R_T = 2.51$ meters. This initial estimation of R is slightly overestimated but close enough to obtain the range of forces that the passive restrainers will have to withstand before breaking. The hoop force given by Eq. (7) is the force on the cylindrical portion of the inflatable per unit of length. The total force acting in the hoop direction of the cylinder is the product of the force given by Eq. (7) and the nominal length ($L = 3.658$ meters) of the cylindrical portion of the inflatable. This product is equal to $F_T = 1652.7$ N, and it is the total active force in the hoop direction that has to be equal to the total reaction force carried out by all the passive restrainers before their breakage. A total of six passive restrainers were installed to control the release of the membrane material stored on the cylindrical portion of the inflatable. These passive restrainers simulate the connectors installed along the first pre-fold shown in Figure 15. Then, by dividing the total force F_T into six passive restrainers, the force that each one will take individually before their breakage at the pressure P_{conn} is equal to F_c = 275 *N*.

Considering that the passive restrainers are typically manufactured from materials that are commercially available, such as synthetic filaments or metallic wires, this work adopted values of individual breakage force in the range of 267 *N* (60 lbf) to 311 *N* (70 lbf) [22]. Since the force per connector was initially estimated using an overestimated radius R, a passive restrainer with a nominal uniaxial breaking strength of $267\ N$ for a maximum elongation of 0.01 m of was adopted for the simulations results presented next.

5.4 Confined Inflation with Controlled Release of Membrane

The simulation of the deployment and inflation implementing a controlled release of the membrane material was similar to the process described previously (Case 0 with an artificial compressive strength of 0.01% of the membrane tensile strength) except for the presence of the passive restrainers modeled with connector elements. Case A included only one pre-fold, and Case B included two pre-folds for controlling the release of the membrane. The simulation results in the last stage of the inflation (from *t* = 245 sec to *t* = 255 sec) corresponding to Cases 0, A and B are illustrated in the cross-sections of Figure 21. The sequence of images of Figure 21 corresponding to each case illustrates cross-sections of the inflatable structure highlighting the different membrane behaviors with and without using the passive restrainers. From Figure 21, it is worth to note that:

- In Case 0, as observed previously, the distribution of the membrane was not uniform around the tunnel perimeter. This non-uniformity is displayed by the presence of folds or wrinkles on the tunnel floor. Moreover, the non-uniform distribution of membrane material led to the formation of uncovered areas or bridging of the membrane material in the two right corners of the tunnel profile.
- In Case A, simulation results show that the inflatable was able to conform to the upper right corner, but it was not able to fill the lower right corner of the tunnel. A comparison between Case 0 and Case A at *t* = 249 seconds shows that the bridging of the membrane on the upper right corner of the tunnel profile is significantly reduced in Case A. The improvement in the local conformity of Case A is attributed to the inclusion of the pre-folded membrane material

stored (single colored band in Figure 21) during the folding process released upon breakage of the passive restrainers.

- In Case B, simulation results show a remarkable improvement in the local conformity in both right corners of the tunnel profile. This improvement is attributed to the inclusion of the two pre-folds described previously, and the sequential release of the membrane contained in both pre-folds (double colored bands in Figure 21) upon breakage of the passive restrainers at the end of the inflation between $t = 249$ seconds and $t = 255$ seconds. Moreover, in the simulation corresponding to Case B, a second set of passive restrainers was used in the third pre-fold shown in Figure 18(c). The number of passive restrainers used in the third pre-fold was calculated taking into account the radius of curvature (R2 shown in Figure 22) of the inflatable in the vicinity of the lower right corner of the tunnel before the breakage of the connectors in Case A. Moreover, the radius of curvature on the lower right corner of the tunnel is about half of the radius of the inflatable (R1) at the onset of the breakage of the passive restrainers of the first pre-fold as illustrated in Figure 22. Considering the practicality of using the same type of passive restrainers used in Case A, and the hoop stresses and corresponding forces calculated from Eq. (7), the second set of passive restrainers included only three units that were installed on the cylindrical portion of the inflatable at the location of the third pre-fold, and placed at the two ends and in the middle of the cylinder.

In order to understand the effects of the inclusion of passive restrainers, the time history of the internal pressure, the internal volume, the axial forces carried out by the different sets of passive restrainers modeled with connector elements, as well as their failure status (where 0 corresponds to no breakage, and 1 corresponds to breakage), are plotted in Figure 23 and Figure 24 for Case A and B, respectively. For Case A, Figure 23 shows the following:

- Similarly to Case 0 (Figure 13), the internal pressure (gauge pressure) remains practically constant and close to zero for about 90% (or $t \approx 240$ seconds) of the inflation process, whereas the internal volume (CVOL) of the inflatable increases linearly during the same interval as illustrated in Figure 23(a).
- A closer look at the pressure history shows that during the initial deployment ($t = 0$ to $t = 2$ seconds), the internal pressure (PCAV) shows the presence of a vacuum effect produced by the unfolding and fall of the inflatable due to the action of gravity, as illustrated in Detail 1-A

of Figure 23(b). The activation of the inflator (at t = 2 seconds) produces a recovery of the internal pressure, and after a few seconds of the activation of the inflator, the internal pressure reaches a positive value but with a magnitude close to zero until $t \approx 240$ seconds.

- Then, between $t \approx 240$ and $t \approx 250$ seconds, the pressure gradually increases until it reaches its first local peak at $t = 249$ seconds. At this time, the internal pressure produces hoop forces that break the passive restrainers. Right after the breakage of the passive restrainers, the membrane contained in the pre-fold is released, causing a small increase in the volume of the inflatable, which produces a drop of the internal pressure as illustrated in Detail 2-A of Figure 23(b). However, since the inflator system continues being active, the continuous addition of air mass flow produces a recovery of the internal pressure until it finally approaches the target final pressure P, while the volume tends to a constant value close to the target value of $V = 108$ m^3 as the inflatable reaches its final position in the tunnel.
- Looking at the time history of the axial forces carried out by the connector elements that represent the passive restrainers, the fluctuation of the forces illustrated in Figure 23(c) can be separated into the following parts. 1) From $t = 0$ to $t \approx 20$ seconds, the forces fluctuated in correspondence to the initial unfolding and positioning of the inflatable in the tunnel section; during this interval, the magnitude of the forces did not exceed 30% of the axial strength assigned to the connector elements. 2) Between $t \approx 20$ seconds and $t \approx 200$ seconds, the inflatable continued its volume expansion, while the axial forces carried out by the connectors remained approximately at a constant load of about 10% of the axial strength assigned to the connector elements. 3) Between $t \approx 200$ and $t \approx 250$ seconds, the connectors start taking more load and are stretched as the inflatable completes its expansion within the tunnel. 4) Then, at $t = 250$ seconds, the internal pressure reaches a local peak of $P = 284$ Pa. At this pressure, the set of six connectors fail nearly simultaneously at an individual force $F = 255$ N which is close to the axial strength assigned to the connector elements. 5) Finally, after the breakage of the connectors, from $t = 250$ to $t = 280$ seconds, the axial forces in the connectors drop to zero since they have exceeded the failure limit and cannot take any additional axial force.

Similarly, from Figure 24 corresponding to Case B, the following observations can be made:

- The overall evolution of internal pressure (PCAV) and the internal volume (CVOL) of the inflatable follows a pattern similar to Case A, as illustrated in Figure 24(a). The vacuum effect at the beginning of the deployment is similar in magnitude and shape to Case A, as illustrated in Detail 1-B of Figure 24(b).

- The variation of internal pressure at the time of breakage of the sets of connector elements is plotted in the Detail 2-B of Figure 24(b). Since Case B included two pre-folds, the pressure history shows two main local peaks followed by two drops of internal pressure right before and right after the breakage of the connectors. The presence of the third small local peak between the two main local peaks indicates that the breakage of the connectors was not simultaneous. However, the inflator, as in Case A, continued providing air mass and filling the internal volume of the inflatable producing a recovery of the internal pressure. During the pressurization stage, as in Case A, the internal pressure increased until it reached its target as the volume tended to a constant value.
- The time history of the forces carried out by the two sets of passive restrainers represented by connector elements is illustrated in Figure 24(c) and includes the following parts: 1) From t = 0 to $t \approx 25$ seconds, as in Case A, it is possible to see a series of fluctuating local peaks originated by the fall of the membrane corresponding to the initial deployment. In this case, the magnitude of the forces did not exceed about 25% of the axial strength assigned to the connector elements; 2) Similarly to Case A, from $t \approx 25$ to $t \approx 200$ seconds, the inflatable continues its expansion and the axial force carried out by the connectors is characterized by oscillations around a constant axial load in the range of 1% to 18% of the axial strength assigned to the connector elements; 3) From $t \approx 200$ to about $t = 245$ seconds, the inflatable started to reach its full shape inside the tunnel, which produced a gradual increase on the internal pressure and the connector elements installed in the first pre-fold started to get stretched producing an increase of the axial force until they reached their maximum capacity at $t = 245.5$ second. At that time, the maximum strength of assigned to the connectors is reached causing their breakage and producing the release of the membrane stored in the first pre-fold as seen in the sequence of images of Figure 21; 4) Then, from $t = 245.5$ to $t \approx 255$ seconds, the inflatable continues its expansion in the tunnel and the second set of connector elements installed for the third pre-fold starts to stretch, there is an increase of the axial force until they reached their maximum capacity at $t = 255$ seconds. At this instant, the maximum strength of the connectors is reached causing their breakage which in turns, produces the release of the membrane stored in the third pre-fold as illustrated in the sequence of images of Figure 21; 5)

Lastly, after the breakage, from t = 255 to t = 280 seconds, the axial forces in the connectors elements drop to zero since they are broken and cannot take any additional axial force.

It is worth to note that the behavior of internal pressure, volume and forces carried out by passive restrainers is similar to the behavior obtained from simulations and experimental observations of the performance of large-scale inflatables deployed from a lateral duct bank as reported in [12-14].

5.5 Global and Local Conformity: Contact Area

To quantify the global and local conformity and to highlight the improvements reached with the implementation of pre-folds and the controlled release of the membrane, the contact areas achieved at the end of the simulations in Cases 0, A and B are plotted in Figure 25. The time history of the contact areas followed a similar pattern for all three cases. There was practically no contact other than the attachment of the inflatable to the tunnel ceiling and part of the tunnel floor during the first 20 seconds of the inflation. As the inflation continued, the contact started to increase gradually until around t ~250 seconds, time at which there is a jump in the magnitude of the contact area that corresponds to the breakage of the passive restrainers and the release of the membrane stored in the pre-folds. Figure 25 also shows that at the end of the simulation, the magnitude of the contact area measured for Cases 0, A and B exceeded the nominal contact (NC) area of the cylindrical portion of the inflatable placed in the tunnel and evaluated considering the cylindrical region having the same radius as the tunnel. The magnitudes of the contact area for each of the cases are summarized in Table 5. This summary also includes the percentages of improvement achieved in the three cases. The improvement in the contact area is attributed to two main factors: 1) The confining effect produced by the tunnel in which part of the spherical end caps become part of the cylindrical portion of the inflatable, and 2) the controlled release of the membrane during the last stage of the inflation process, which also contributed to achieving a better local conformity of the membrane material around the tunnel corners and thus, produced an increase in the magnitude of the contact area.

The percentages of improvement due to confining effect are calculated taking into account the nominal contact (NC) area of the cylindrical portion of the inflatable in the tunnel and then comparing this value of the contact area of corresponding to Case 0, which did not include any pre-folds or passive restrainers. The confining effect of the tunnel perimeter, as well as the oversizing of the inflatable, produced an increase of 5.4% in the contact area. For Case A, the inclusion of one pre-fold combined with one set of passive restrainers to control the release of the membrane stored in the pre-fold produced an increase of 15.8% in the contact area with respect to the NC case. For Case B, the addition of two pre-folds and two sets of passive restrainers to control the release of the membrane in the corners of the tunnel produced an increase of 16.6% in the contact area with respect to the NC. These increases in the percentages of the contact area are attributed to the better level of local conformity achieved in the corners of the tunnel as illustrated in the sequence of images of Figure 21. These results also underline the viability of the proposed methodology for implementation in more intricate tunnel profiles where the sealing capacity of the inflatable can be improved by systematic control of the membrane release at critical locations.

5.6 Mass Scaling and Damping: Verification for Confined Inflation

As indicated in Section 3.2, a mass scale factor MSF = 100 was initially adopted for the simulation of confined inflations corresponding to Cases 0, A and B presented in the previous sections. Considering that the weight of the membrane drives the initial deployment from the ceiling of the tunnel section, it is important to understand how the selection of the MSF influences the behavior of the membrane, particularly during the first few seconds when the folded membrane is suddenly released from the storage area and unfolds by its self-weight. In order to characterize the behavior of the different phases of the deployment and inflation process, the kinetic to internal energy (KE/IE) ratio was used here again to identify the regions where the process can be considered dynamic or quasi-static. As mentioned earlier, the behavior of a system is considered quasi-static if the KE/IE ratio is typically below 5% to 10% [15].

Two values of MSF were selected for this study: MSF = 100 and MSF = 1.1. The MSF = 1.1 was selected as a minimum value in order to overcome the no convergence of the simulations for MSF =1.0 due to the influence of severely distorted elements resulting from the folding process, which controlled the calculation of the stable time increment. The time histories of KE/IE ratios were computed for Cases 0, A and B for MSF = 100 and Cases 0 and A for MSF = 1.1, and are illustrated in Figure 26(a) and 26(b), respectively. The same level of damping ($\alpha = 0.2$) was used for both mass scaling factors. Results plotted in Figure 26(a) show three distinctive regions for the time history KE/IE ratios. The first region corresponds to the Initial Deployment, from $t = 0$ to $t \approx 20$ seconds for MSF = 100, with relatively high kinetic energy corresponding to the initial unfolding and fall of the inflatable from the ceiling of the tunnel. The unfolding is induced by its self-weight first, and then by the activation of the inflator (2-second delay) until the inflatable reaches the tunnel floor and the kinetic energy is reduced to nearly zero. The second region corresponds to the Volume Expansion by the action of the inflator. Most of the expansion occurs between $t \approx 20$ to $t \approx 240$ seconds, and it is characterized by a near-to-zero KE/IE ratio mainly originated by the near-to-zero zero kinetic energy produced by the inflator since it occurs at a relatively low air mass flow rate (0.48 kg/sec). The third region, between $t \approx 240$ to $t = 280$ seconds, corresponds to the Final Positioning in which the inflatable reaches the lateral walls and duct bank of the tunnel perimeter with relatively small local peaks of kinetic energy corresponding to the release of the membrane stored in the pre-folds. The same regions are present in the energy ratio time histories corresponding to MSF = 1.1 plotted in Figure 26(b), with the main difference being in the duration of the initial deployment.

For the cases with an MSF = 100, the initial deployment takes between 15 to 20 seconds. This behavior is attributed to the presence of inertial effects originated by the artificial mass scaling. Since the inertial effects act in the opposite direction of the applied force (the weight of the inflatable), their increase produces a decrease on the effect of the gravity acceleration that drives the free fall of the folded inflatable causing a reduction in the amplitude of the kinetic energy. This effect produces an extension on the duration of the initial deployment of the inflatable as seen in the first 20 seconds of Figure 26(a). In other words, an MSF = 100 slowed down the unfolding of the inflatable.

On the other hand, for MSF = 1.1, the initial deployment takes between 1 to 5 seconds, resulting in a faster falling of the membrane material, which in turn increases the kinetic energy and thus, increases the energy ratio in a short period (less than 2 seconds). In other words, a smaller mass scaling factor such as MSF = 1.1 seems to speed up the initial unfolding of the inflatable as no inertial effects are present. Moreover, for both MSFs under consideration, the threshold energy ratio of 10% was exceeded by about 1.3 to 4.8 times during the initial deployment confirming the dynamic nature of the process. From an overall look at the results presented in Figure 26, it can be concluded that except for the initial deployment, the volume expansion and the final positioning of the inflatable are quasi-static processes. A higher mass scale factor does not affect the membrane behavior as the inflation process is completed and it also contributes to significantly decrease the computational time to achieve the same result at the end of the inflation process. Using a workstation with eight processors, parallelization and double precision, the computational times ranged from nearly 840 hours (~35 days) for MSF = 1.1, to 76 hours (~3 days) for MSF = 100. In the case of MSF = 1.1, a few hundred, small and poorly shaped membrane elements resulting from the folding process, controlled and maintained the stable time increment in the order of $1 \cdot 10^{-6}$ to $1 \cdot 10^{-7}$ seconds, which resulted in an unreasonable long computational time. On the other side, the MSF = 100 increased the stable time increment to the order of $1 \cdot 10^{-4}$ to $1 \cdot 10^{-5}$ seconds which contributed to complete the simulation of inflation within an acceptable time.

Furthermore, considering that the only portion of the process that can be considered truly dynamic is the initial deployment, a parametric study was performed to further understand the influence of the MSF in combination with the mass-proportional damping factor α. These factors ranged from $\alpha = 0.0$ (no damping) to $\alpha = 1.0$, with increments of 0.2. These damping factors were implemented for Case 0 (no connectors, simple folding) and Case A (a single line of connectors and a more compact folding), and for MSF = 1.1 and MSF = 100. For these values of MSF and α, and also in correspondence with the zones identified in Figure 26, the initial 15 seconds of the initial deployment were simulated. The KE/IE ratio was used here again to monitor the response as the values of damping and mass scaling changed.

The results summarized in Figure 27 indicate that for a MSF = 1.1, as expected, increasing values of the factor α produced a proportional decrease in the amplitude of the peak KE/IE ratios. Also for a MSF = 1.1, and for Cases 0 and A, the peak kinetic energy is reached during the first two seconds of the deployment. For these two cases, the overall response does not seem to be very sensitive to the changes in the damping factor. This is illustrated in the sequence of images presented in Figures 28 for Case 0, and in Figure 29 for Case A, both compared to the experimental result of [8]. From these two set of images, it can be seen that the response is practically similar for the two damping factors located at the ends of the range considered for the analysis ($\alpha = 0.0$ and 1.0). For these two damping factors, the behavior of the membrane as it deploys is practically the same.

On the other side, looking at Figure 27 for a MSF = 100, for no damping ($\alpha = 0.0$) or relatively lower levels of damping ($\alpha = 0.2$ to 0.4), are significantly affecting the peak energy ratio and duration of the dampening effect. Increasing values of α (from 0.6 to 1.0) seem to compound the inertial effects associated with a higher mass scale factor resulting in a non-realistic overdamped response. The sequence of images of Figures 28 and 29 illustrate this effect for Cases 0 and A, respectively, for no damping, $\alpha = 0.0$, and for $\alpha = 0.2$, which was the value adopted for the simulations presented in the previous sections of this work. Looking at the overall shapes of the inflatable as it unfolds, it seems that the combination of inertial effects associated with the implementation of a relatively large MSF along with a relatively low level of damping (say α = 0.0 to 0.2) produces a better representation of the experimental results. The slight delay seen in the initial unrolling of the experimental prototype may be attributed to a degree of bonding developed on the surface of the folds due to the type of coating of the fabric used to manufacture the inflatable. A priori, the magnitude of this apparent bonding is not simple to quantify and to implement in the simulation models. But the adoption of a relatively high MSF along with a low level of damping seems to be able to capture that effect without significantly distorting the overall behavior at an acceptable computational cost.

Overall, looking at all the results presented in this section, and considering that most of the inflation sequence is a quasi-static process, it is clear that if further parametric studies were necessary to test other folding configurations, or airflow rates for achieving different inflation time targets, or for testing other features in the inflatable or the tunnel perimeter, the adoption of smaller values of MSFs would be impractical.

6. Conclusions

A procedure for simulating a controlled deflation, folding, deployment, and inflation of a large-scale inflatable structure for sealing a tunnel cross-section has been presented. The simulation steps of the proposed procedure can closely reproduce the steps of the work implemented experimentally including the preparation of the inflatable, installation in the tunnel section as well as the initial deployment and inflation. The simulation results are in good agreement with experimental results reported in the literature and are helpful to predict the performance of the inflatable and minimize future experimental iterations for similar or new configurations.

The implementation of controlled deflation techniques with the addition of pre-folds held by passive restrainers produced a significant improvement in the resultant deflated shape producing the reduction in the amplitude of wrinkles and also improving the distribution of the membrane over the surface of the resultant deflated shape. This technique also contributed to reducing the thickness of the folded inflatable when installed on the ceiling of the tunnel profile by about 44%.

The inclusion of passive restrainers contributed not only to preserve the position of the pre-folds during the folding procedure but also to produce a gradual release of the membrane during the latter stages of the inflation process. Simulation results showed the gradual release of the membrane material during the inflation contributed to reaching higher levels of local conformity by closing gaps in critical corners of the tunnel perimeter, which translated in an increased contact area by 15.8% to 16.6%.

Simulation results also showed that the simplified geometry of the inflatable adopted for the simulations presented in this work could reach similar levels of global and local conformity as the levels reached with a fitted shape of the inflatable used in previous experimental evaluations. The influence of the mass scaling factor (MSF) and damping were examined to understand their effects on the computational time while still representing the experimental results. For the geometric design and material properties of the inflatable examined in this work, a value of MSF equal to 100, along with a mass-proportional damping factor $\alpha = 0.2\ s^{-1}$, were found to provide a good compromise between computational time and computational results that were in close agreement with experimental observations.

Finally, the simulation results presented in this work suggest that with the appropriate selection of simulation parameters such as mass scaling factor, artificial compressive strength and damping, as well as the implementation of controlled deflation, inclusion of pre-folds and passive restrainers, an inflatable with a cylindrical shape can be adapted to conform to more intricate tunnel profiles and produce improvements on the contact area, which ultimately translates into a better sealing capacity of the inflatable plug.

Acknowledgments

The authors would like to acknowledge the SIMULIA brand of Dassault Systemes for providing the SIMULIA Academic Research Suite license used in this work.

References

[1] The Blue Ribbon Panel on Bridge and Tunnel Security, Recommendations for Bridge and Tunnel Security. Publication FHWA-IF-03-036. U.S. Department of Transportation, 2003.

[2] TCRP Report 86/NCHRP Report 525, Public Transportation Security. Volume 12. Making Transportation Tunnels Safe and Secure. Transportation Research Board of the National Academies, Washington, D.C., 2006.

[3] N. Rabkin, Passenger Rail Security, Federal Strategy and Enhanced Coordination Needed to Prioritize and Guide Security Efforts. Publication GAO-07-583T, U.S. Government Accountability Office, 2007.

[4] R. R. Inouye, J.D. Jacobazzi, The Great Chicago Flood of 1992. Civil Engineering ASCE 62(11) (1992) 52-55.

[5] R. Zimmerman, Planning restoration of vital infrastructure services following Hurricane Sandy: Lessons Learned for Energy and Transportation. J. of Extreme Events, 19 1(1) 145004 (2014) 1-38.

[6] E.J. Barbero, E.M. Sosa, X. Martinez, J.M. Gutierrez, Reliability Design Methodology for Confined High-Pressure Inflatable Structures. Engineering Structures, 51 (2013) 1-9.

[7] E.M. Sosa, G.J. Thompson, E.J. Barbero, Testing of full-scale inflatable plug for flood mitigation in tunnels. Transportation Research Record: J. of the Transportation Research Board, 2407(2) (2014) 59-67.

[8] X. Martinez, J. Davalos, E.J. Barbero, E.M. Sosa, W. Huebsch, K. Means, L. Banta, G.J. Thompson, Inflatable Plug for Threat Mitigation in Transportation Tunnels. Pr. of the Society for the Advancement of Material and Process Engineering (SAMPE) Conference, Baltimore, MD, May 21-24, 2012.

[9] H. Fountain, Holding Back Floodwaters with a Balloon. The New York Times/Science 3 Supplement. https://www.nytimes.com/2012/11/20/science/creating-a-balloonlike-plug-to-hold-back-floodwaters.html., 2012 (accessed July 20, 2018).

[10] E.J. Barbero, E.M. Sosa, G.J. Thompson, Testing of Full-Scale Confined Inflatable for the Protection of Tunnels. Pr. of the VI International Conference on Textile Composite and Inflatable Structures, Structural Membranes 2013, Munich, Germany, October 9-11, 2013.

[11] E.M. Sosa, G.J. Thompson, E.J. Barbero, S. Ghosh, K.L. Peil, Friction Characteristics of Confined Inflatable Structures. Friction, 2(4) (2014) 365–390.

[12] E.M. Sosa, G.J. Thompson, E.J. Barbero, Experimental Investigation of Initial Deployment of Inflatable Structures for Sealing of Rail Tunnels. Tunneling and Underground Space Technology, 69 (2017) 37-51.

[13] E.M. Sosa, J.C. Wong, A. Adumitroaie, E.J. Barbero, G.J. Thompson, Finite Element Simulation of Deployment of Large-Scale Confined Inflatable Structures. Thin-Walled Structures, 104 (2016) 152-167.

[14] E.M. Sosa, J.C. Wong, E.J. Barbero, Confined Inflatable Structures: From Experiments to Simulations. Pr. of the XXII Congreso Sobre Métodos Numéricos y sus Aplicaciones, ENIEF 2016, Argentine Association For Computational Mechanics (AMCA), Córdoba, Argentina, November 8-11 (2016) 313-330.

[15] Abaqus User's Manual, Documentation Collection Version 6.14-2. Dassault Systemes Simulia Corp., Providence, RI, 2014.

[16] Altair HyperWorks 14.0. Altair HyperCrash: Altair HyperCrash Capabilities. Altair Engineering, Inc. Troy, MI, 2016.

[17] J.C. Molina, Mechanical Characterization of Fabrics for Inflatable Structures, M.S. Thesis, Morgantown, WV, 2008.

[18] L. Zhang, Off-Axial Tensile Properties of Preconstraint PVDF Coated Polyester Fabric Under Different Tensile Rates. Advances in Materials Science and Engineering, Volume 2016, Article ID 9856474. http://dx.doi.org/10.1155/2016/9856474, 2016 (accessed July 20, 2018).

[19] C. Galliot, R.H. Luchsinger, A New Test Method for the Investigation of Coated Fabric Shear Behavior. Tensinews, 20 (2011) 8-9.

[20] Air Properties Definitions. NASA, Glenn Research Center. https://www.grc.nasa.gov/www/k-12/airplane/airprop.html, (accessed November 16, 2017).

[21] B.G. Kyle, Chemical Process Thermodynamics, 3rd Ed., Phi, Delhi, India, 2000.

[22] Spectra Fiber, Fishing Line. https://www.honeywell-spectra.com/applications/fishing-line/, (accessed November 16, 2017).

[23] S.R. Wu, L. Gu, Introduction to the Explicit Finite Element Method for Nonlinear Transient Dynamics. John Wiley & Sons, Inc., Hoboken, New Jersey, 2012.

[24] A.R.G. Della Pietra. Lezioni di Meccanica Applicata alle Macchine, Vol. 1. Naples, Italy, 1990.

FIGURES

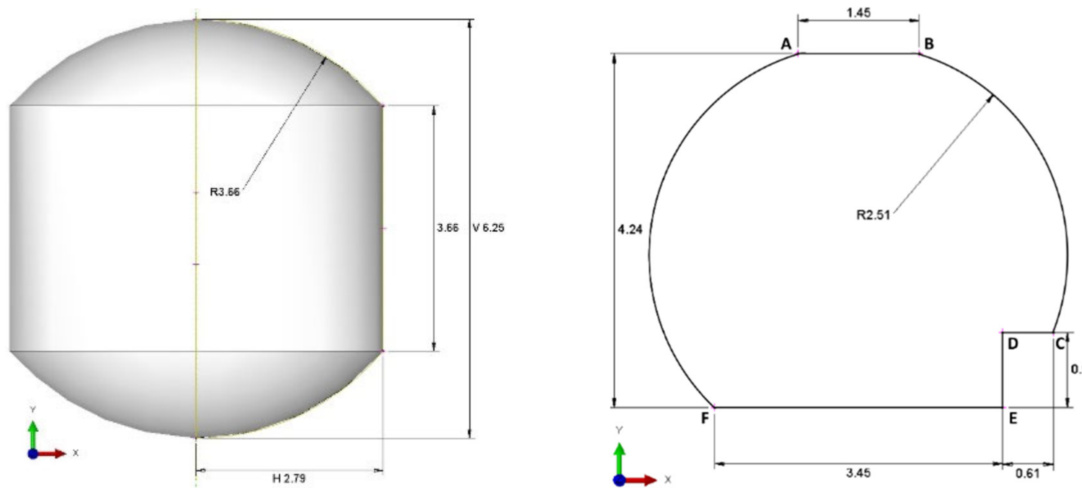

(a) (b)

Figure 1. Geometries and dimensions: (a) Inflatable structure; (b) Tunnel cross-section. Dimensions in meters.

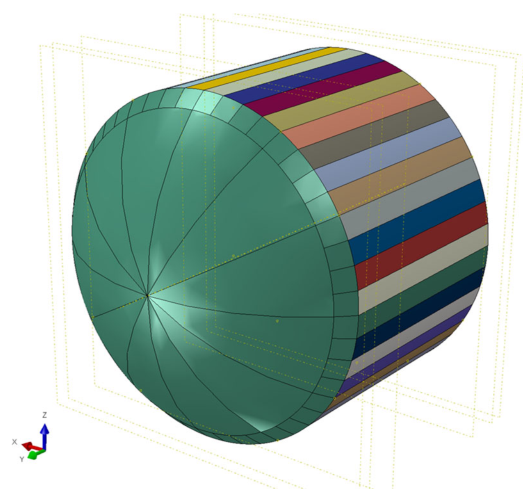

Figure 2. Inflatable structure, FE initial geometry, and partitions generated using Abaqus/CAE.

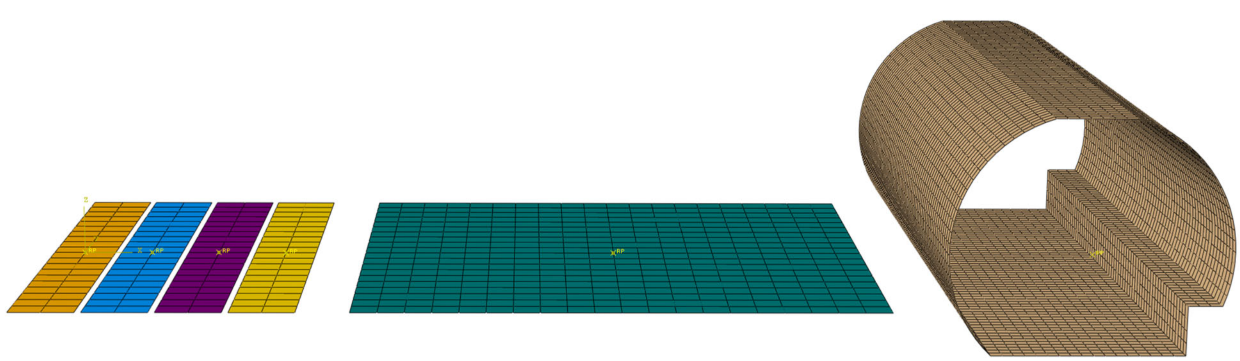

(a) (b) (c)

Figure 3. Meshes of folding planes (a), base (b) and tunnel segment (c).

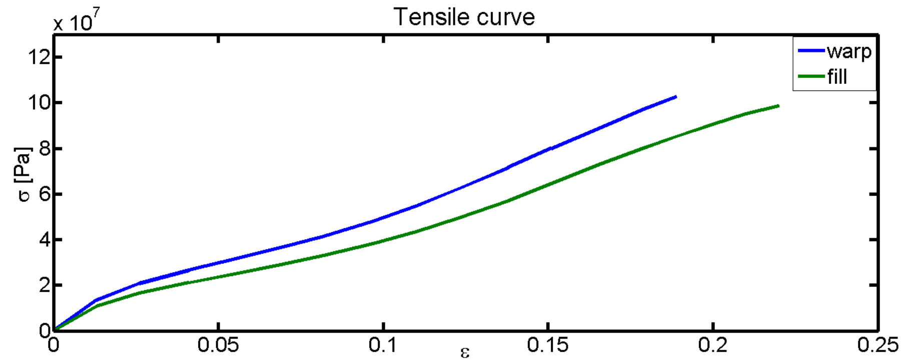

(a)

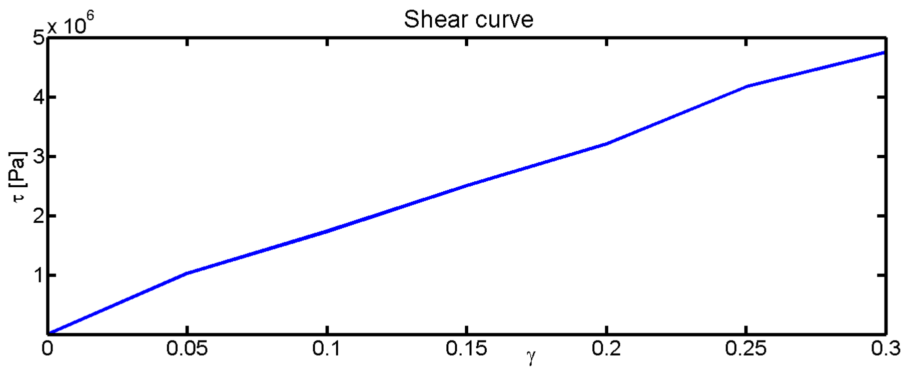

(b)

Figure 4. Constitutive model of fabric material: (a) Mechanical behavior under tensile load (adapted from [17, 18]); (b) Mechanical behavior under shear load (adapted from [19]).

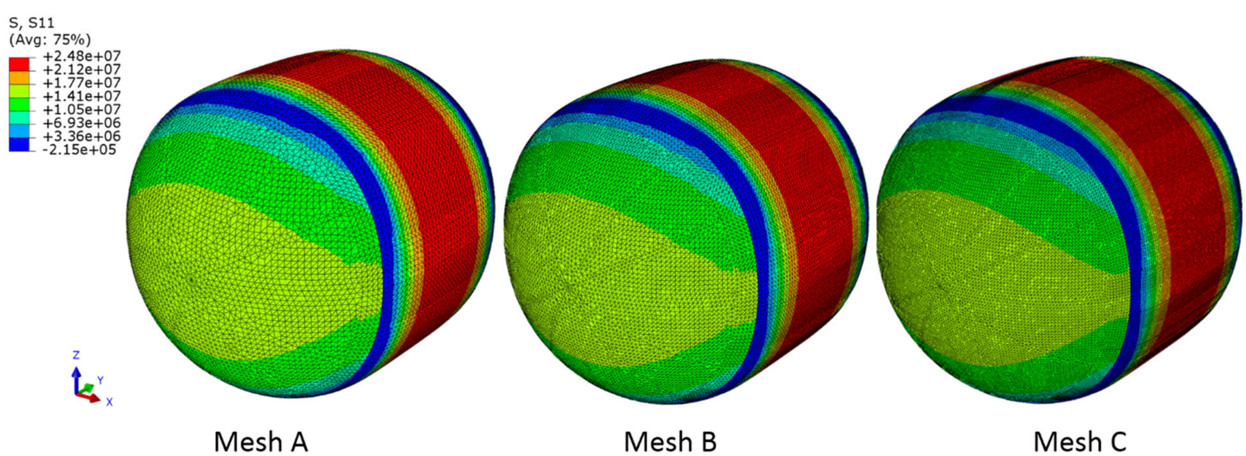

Figure 5. Hoop stress distribution for different mesh densities.

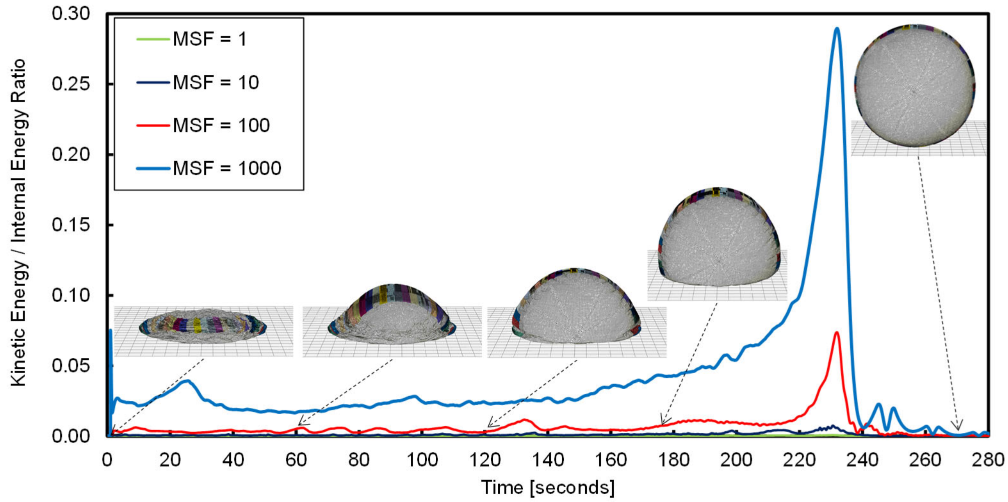

(a)

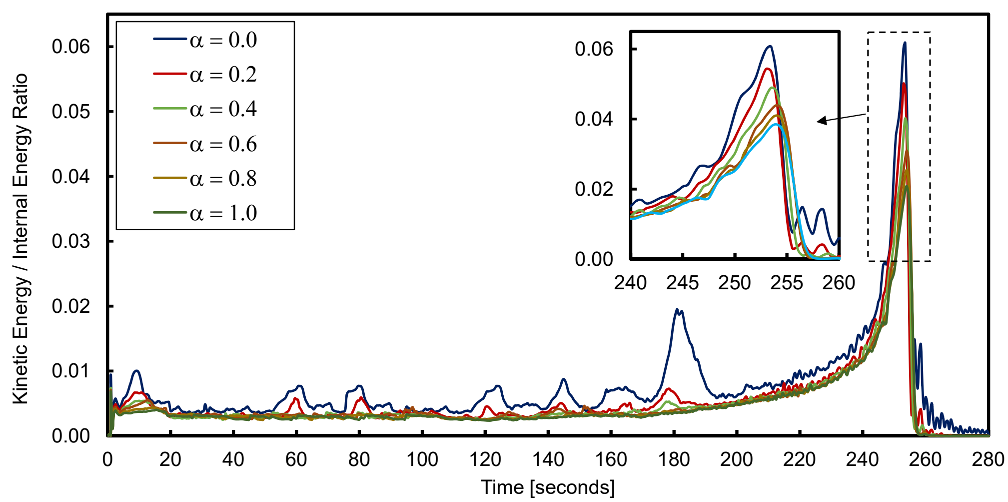

(b)

Figure 6. Unconfined inflation. Time histories of kinetic energy to internal energy ration (KE/IE) for: (a) Different values of Mass Scaling Factor (MSF), no damping; (b) Different values of mass-proportional damping α, for a constant MSF = 100.

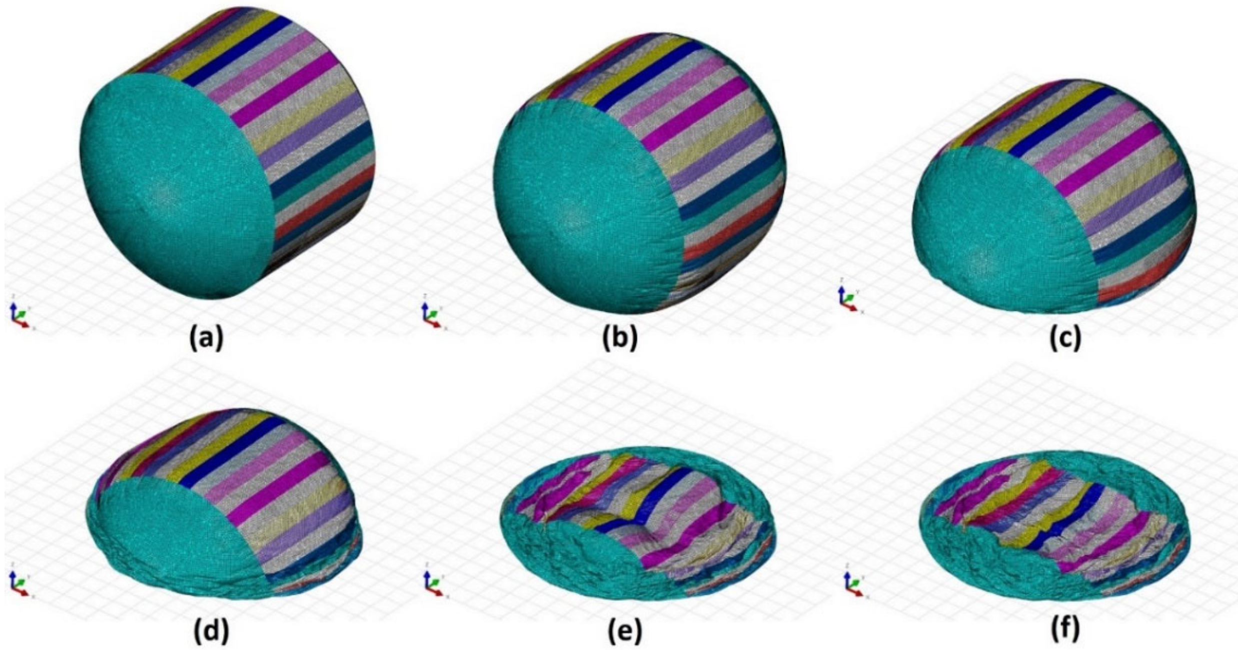

Figure 7. Case 0. Sequence of controlled deflation.

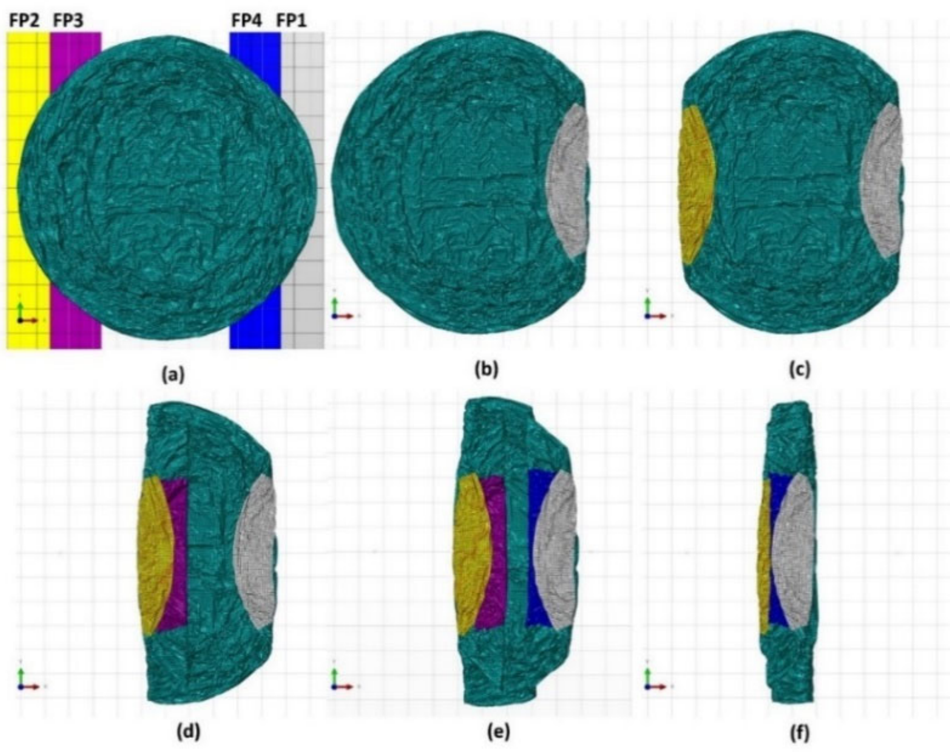

Figure 8. Case 0. Folding sequence, main folding steps, top view (folding planes removed for clarity in images (b) to (f)).

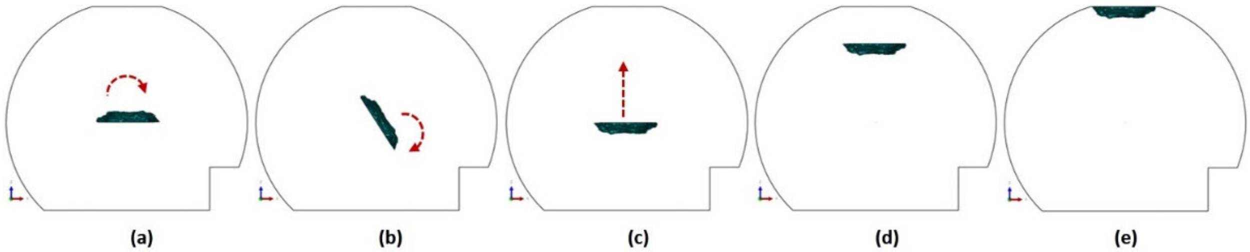

Figure 9. Case 0. Sequence of placement of folded inflatable in the tunnel section.

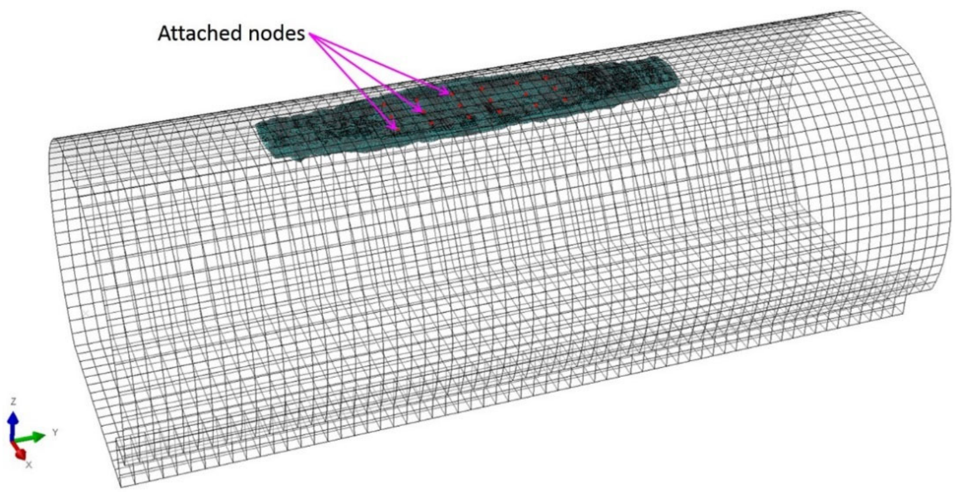

Figure 10. Detail of the attached lines on the ceiling of the tunnel.

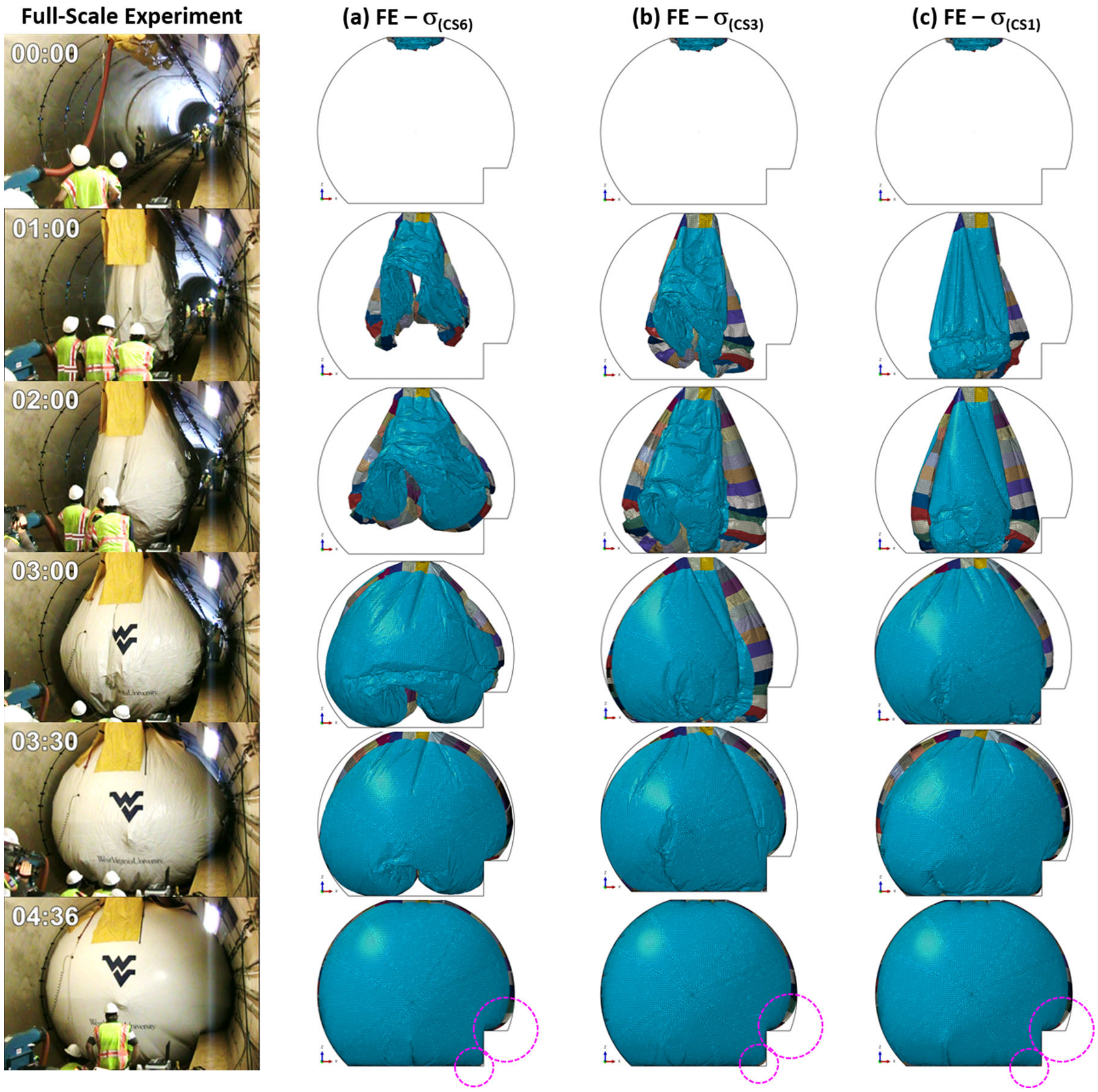

Figure 11. Case 0. Results of the FE Model compared to full-scale experiment [8]. Influence of membrane artificial compressive strength. Comparison of simulation results for: $\sigma_{CS6} \sim 0.5\%\ \sigma_{max}$; $\sigma_{CS3} \sim 0.05\%\ \sigma_{max}$; and $\sigma_{CS1} \sim 0.01\%\ \sigma_{max}$.

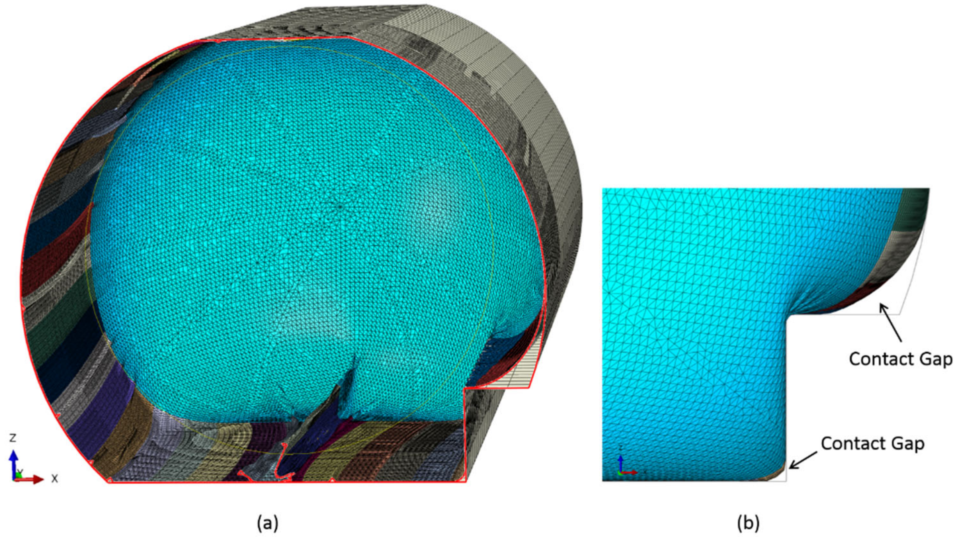

Figure 12. Case 0. FE Model: (a) Detail of wrinkles on the tunnel floor; (b) Detail view of lack of local conformity.

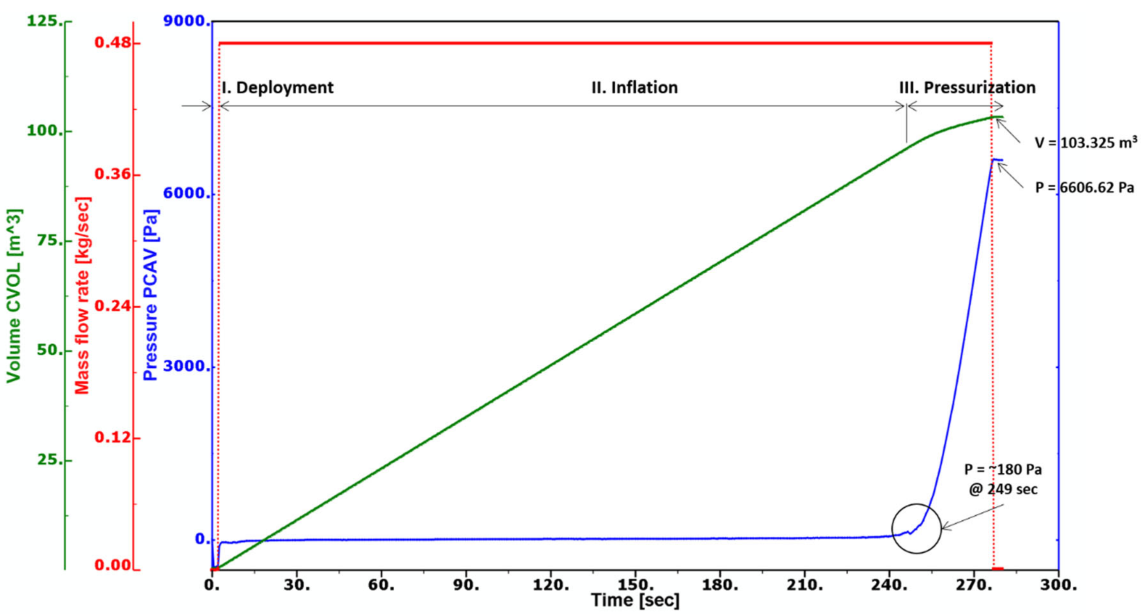

Figure 13. Case 0. Time history of gauge pressure, internal volume for an air mass flow rate.

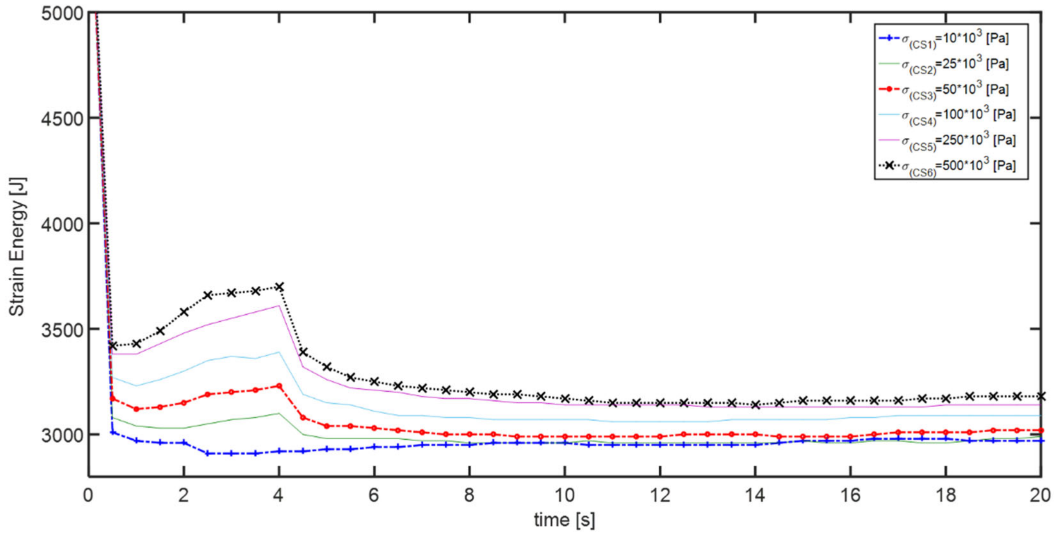

Figure 14. Time history of strain energy (SE) for different values of membrane artificial compressive strength.

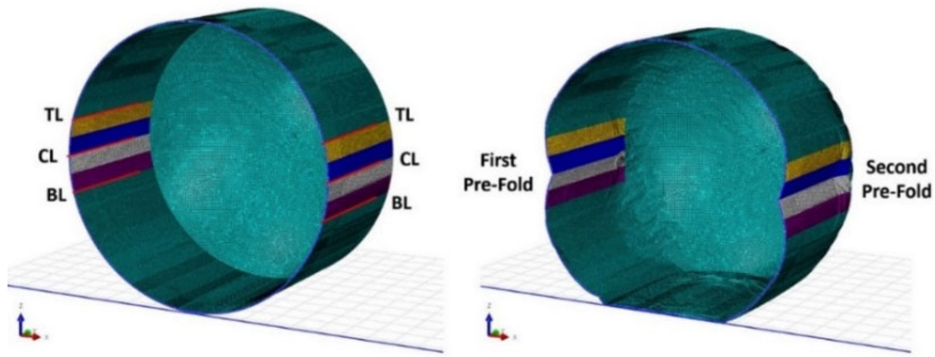

Figure 15. Case A. Controlled deflation, reference lines (TL top line, CL center line, BL bottom line).

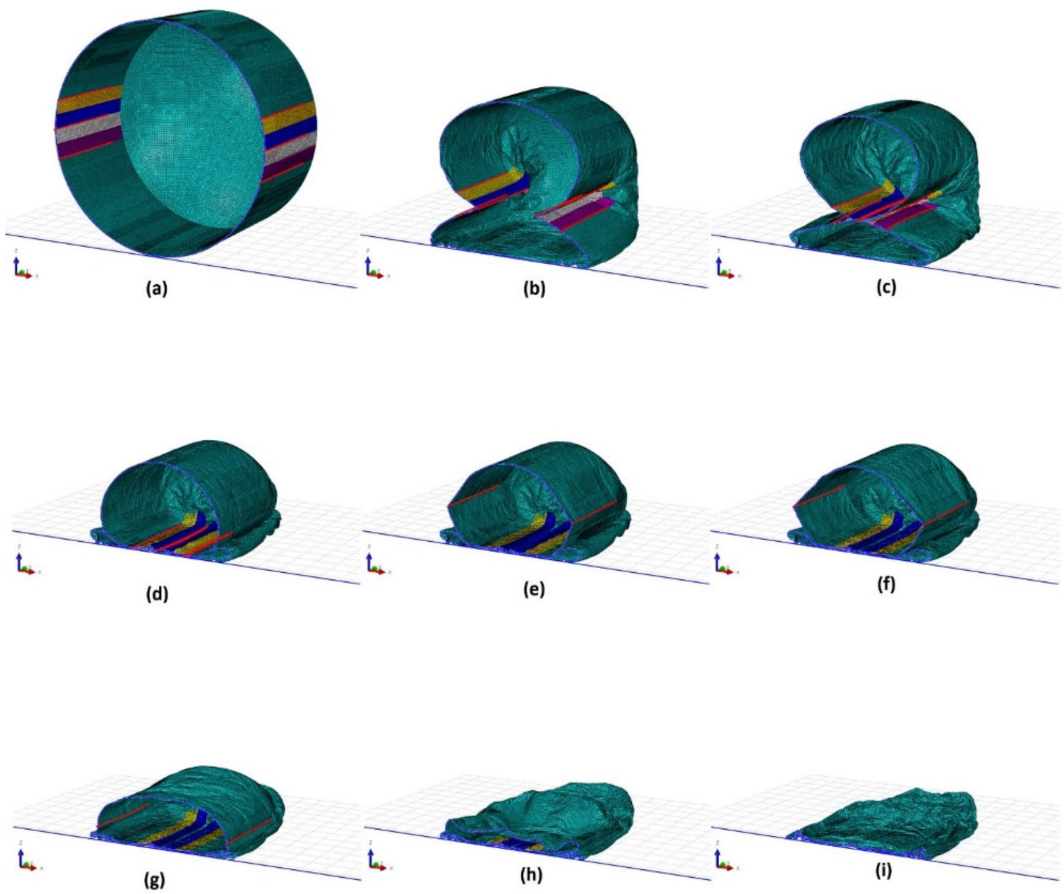

Figure 16. Case A. Sequence of controlled deflation with the addition of pre-folds.

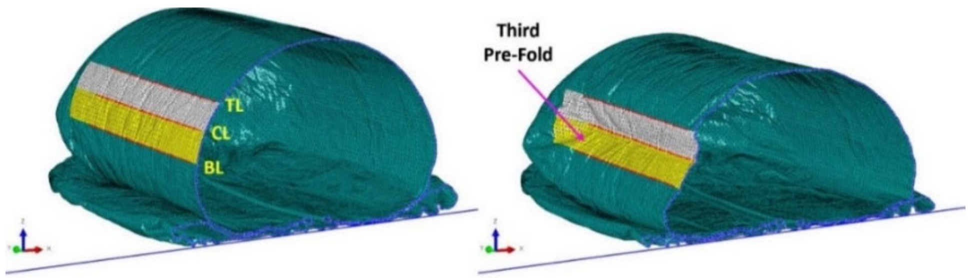

Figure 17. Case B. Controlled deflation, reference lines (TL top line, CL center line, BL bottom line) and the position of pre-folds.

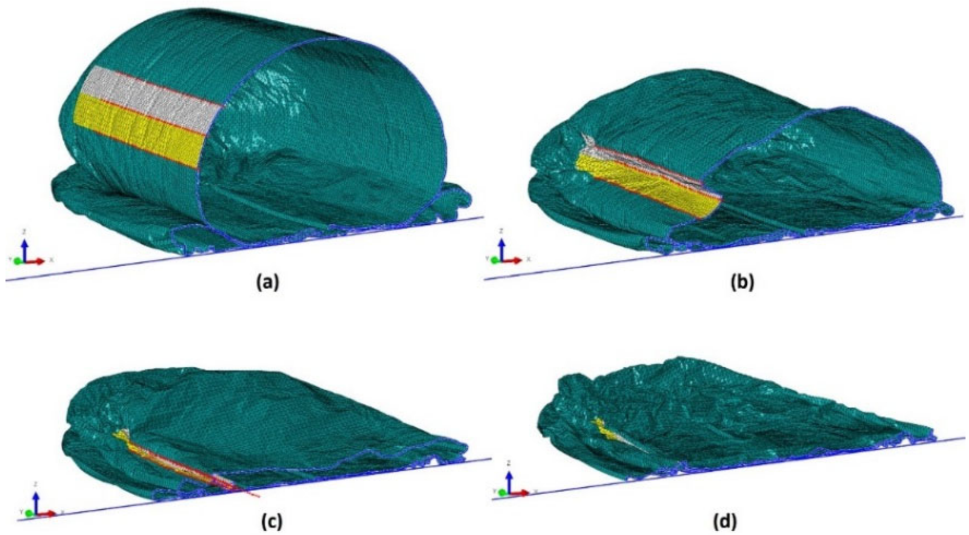

Figure 18. Case B. Sequence of controlled deflation the addition of a third pre-fold.

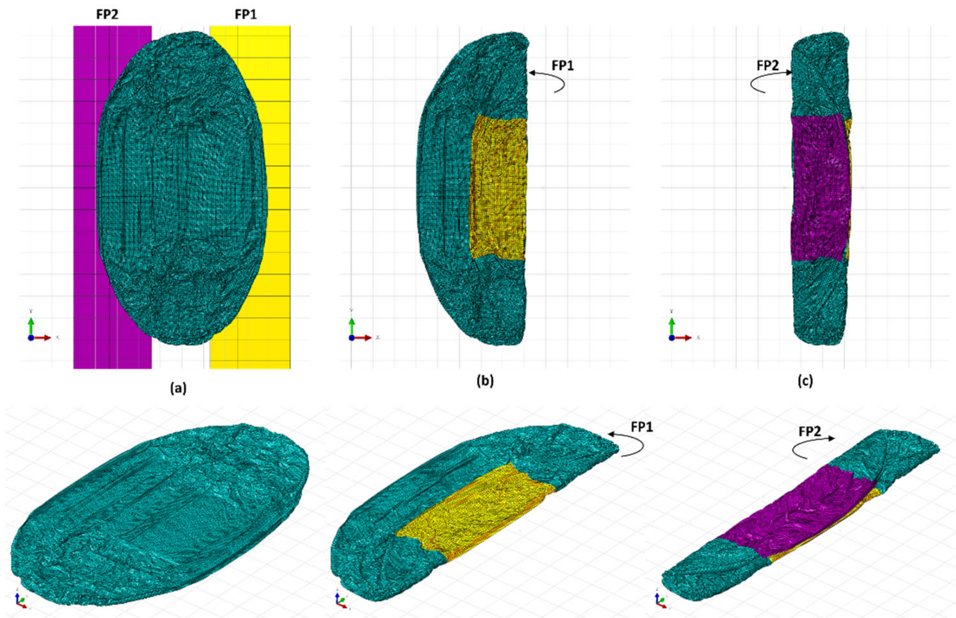

Figure 19. Cases A and B. Folding sequence, main folding steps, top and isometric views (folding planes removed in (b) and (c) for clarity).

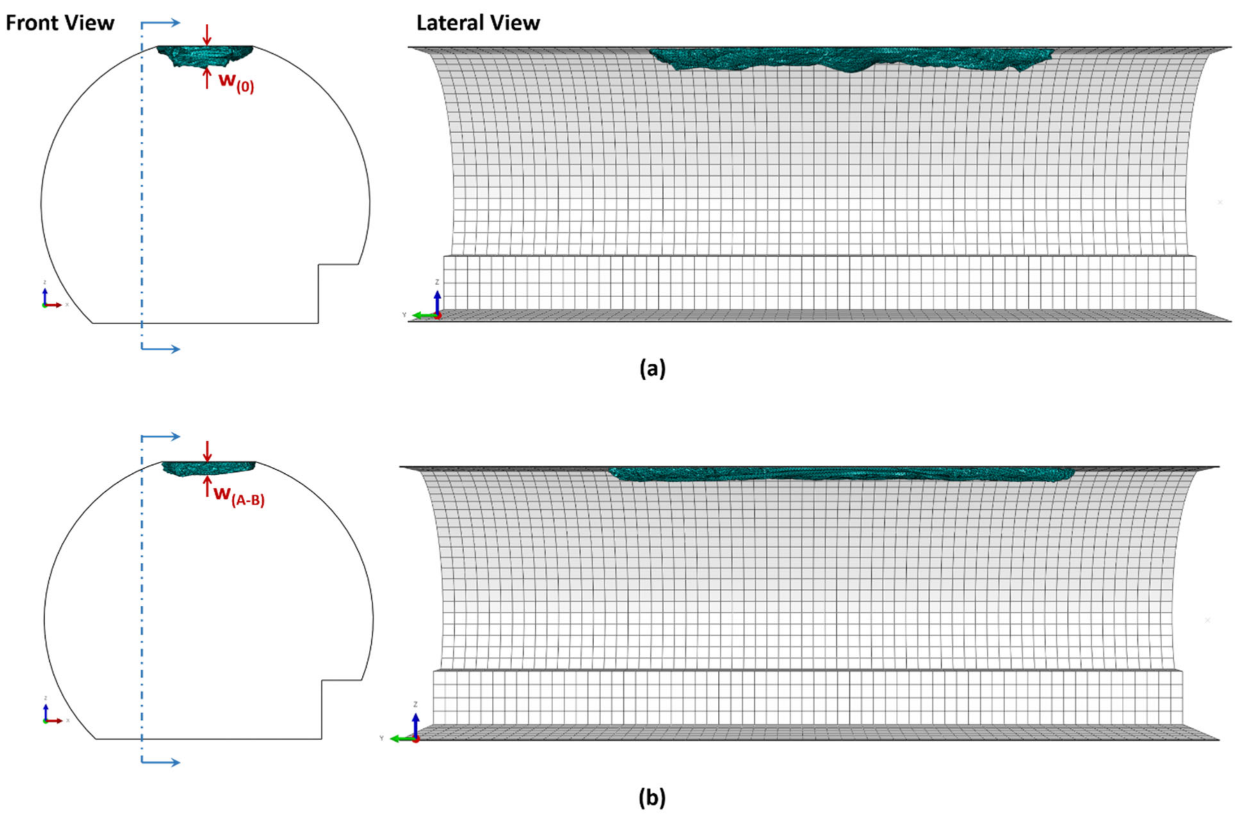

Figure 20. (a) Folded shape without pre-folds (Case 0); (b) Folded shape including pre-folds (Cases A and B).

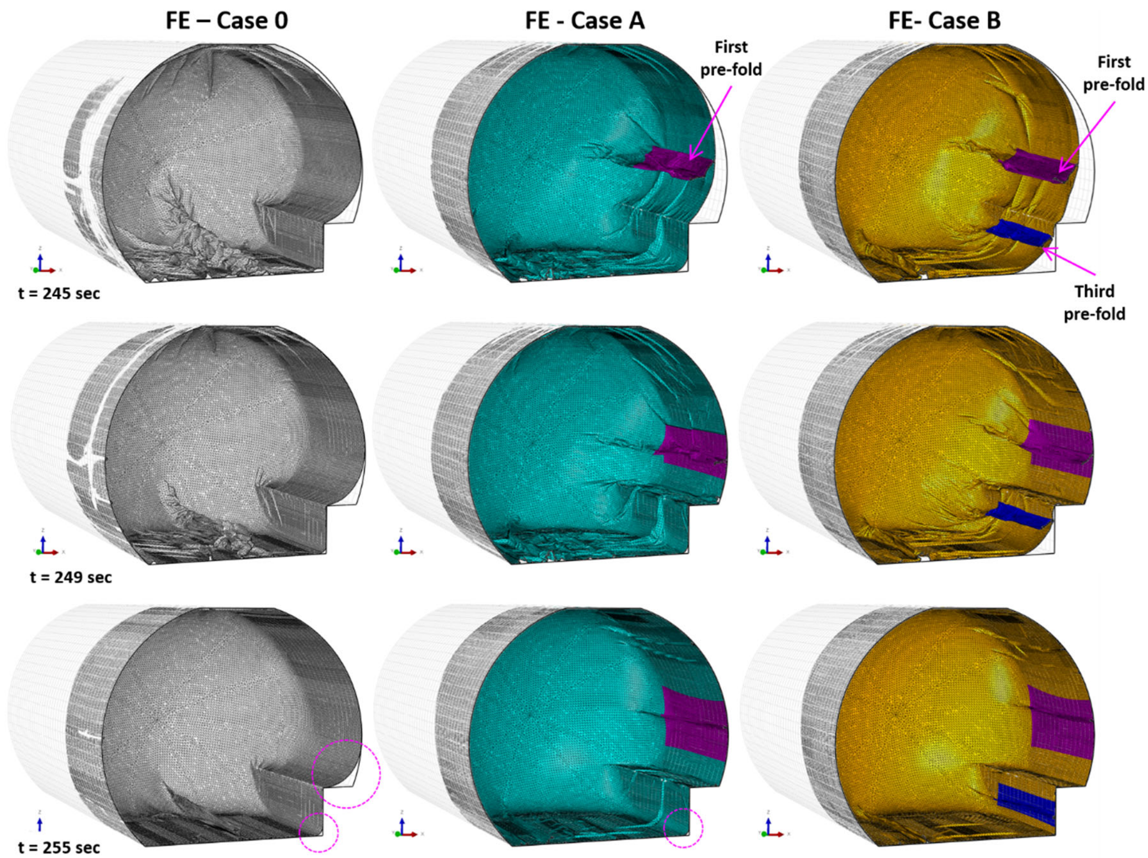

Figure 21. Controlled release of the membrane, simulation results for Cases 0, A and B.

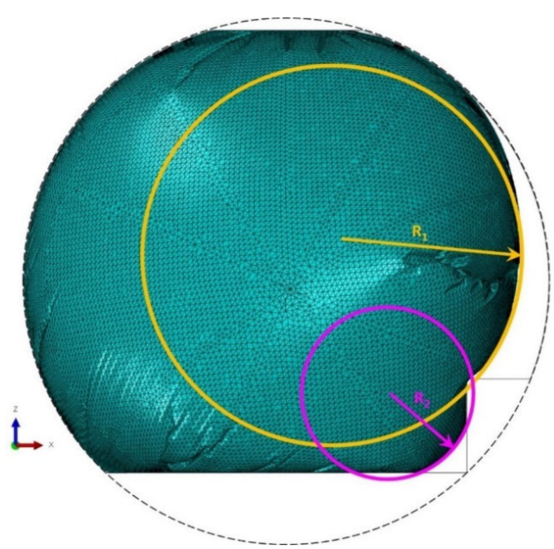

Figure 22. Estimated radii of curvature of inflatable at the onset of failure of passive restrainers.

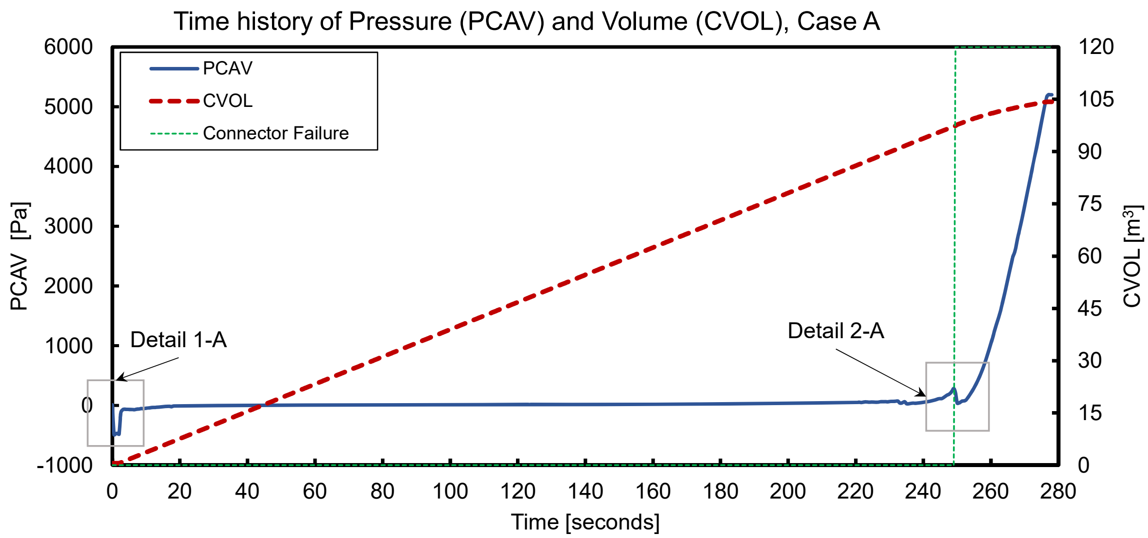

(a)

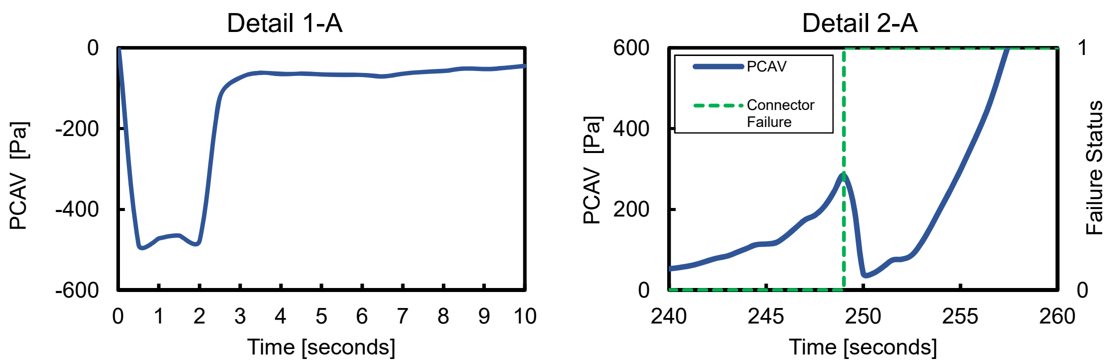

(b)

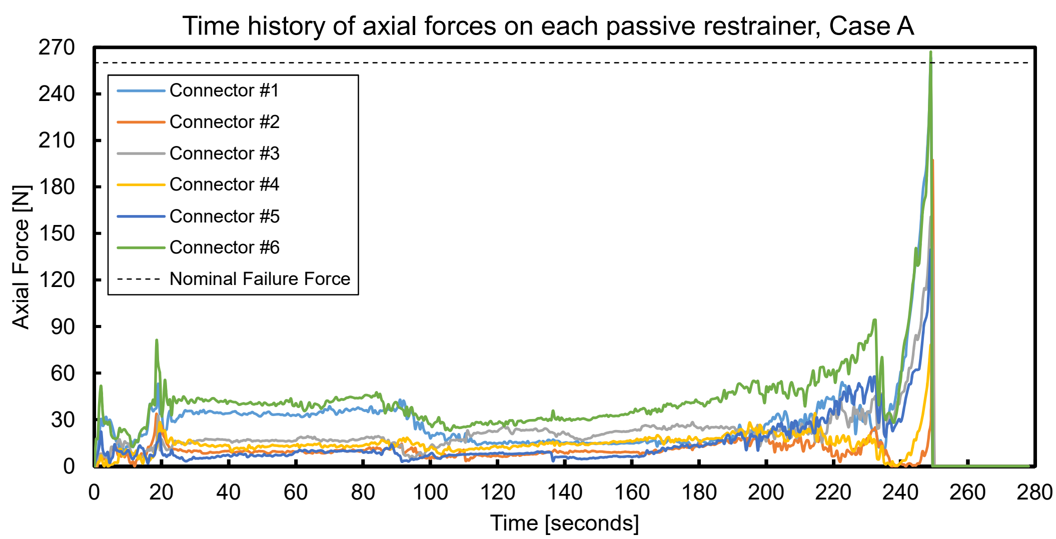

(c)

Figure 23. Case A. Time history of (a-b) gauge pressure, internal volume, and failure status; (c) axial forces carried out by passive restrainers.

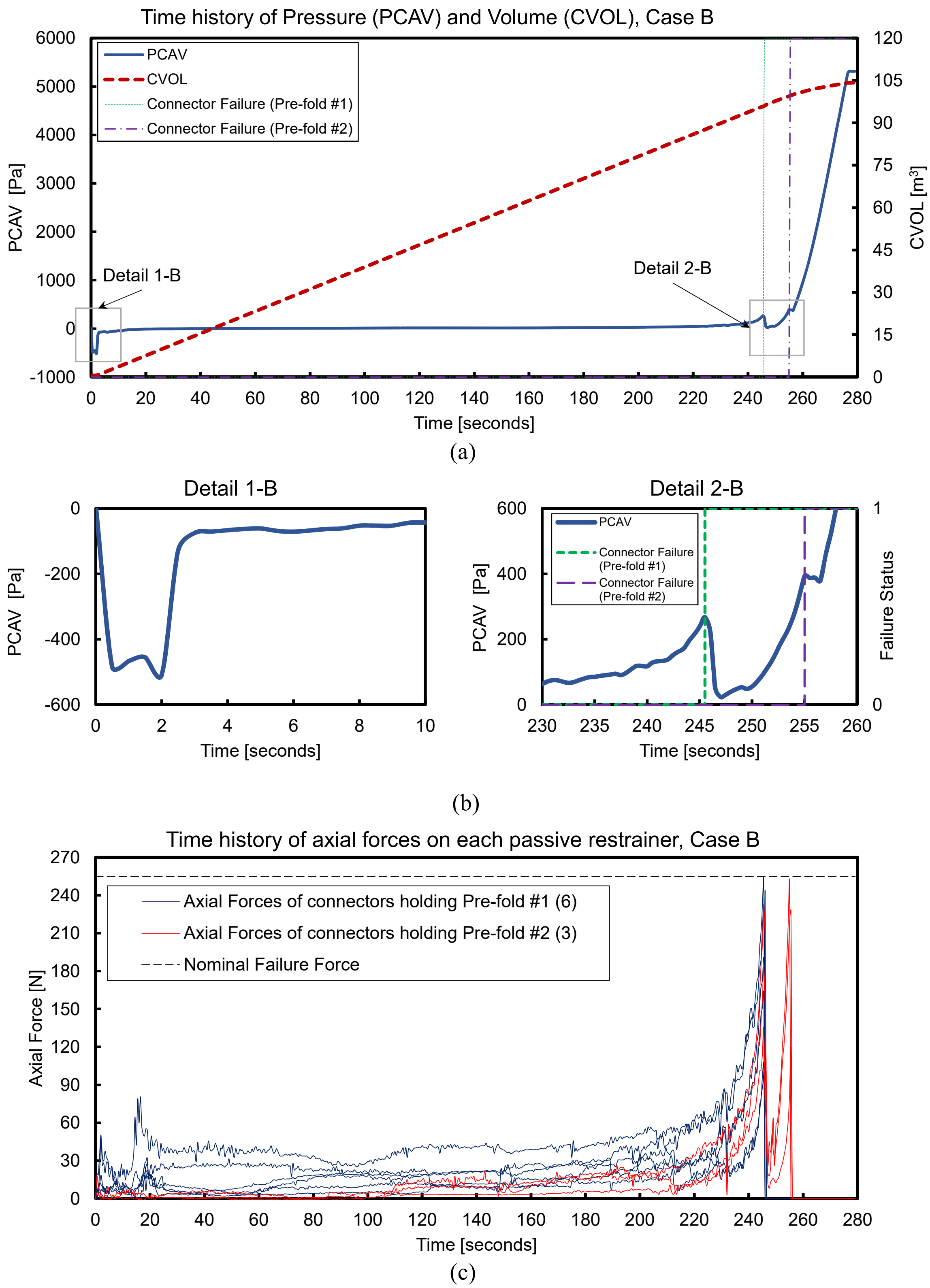

Figure 24. Case B. Time history of (a-b) gauge pressure, internal volume, and failure status; (c) axial forces carried out by passive restrainers.

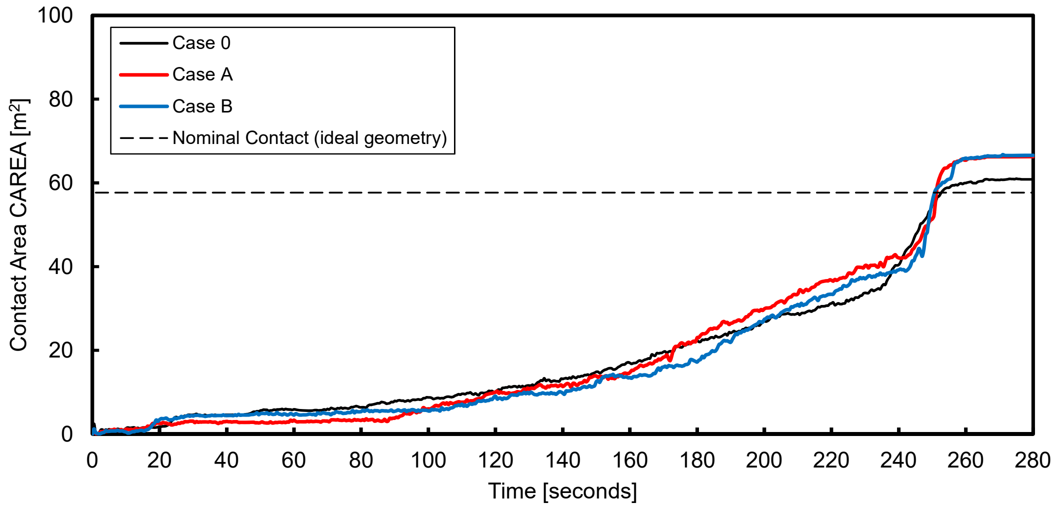

Figure 25. Time history of contact area for Cases 0, A and B.

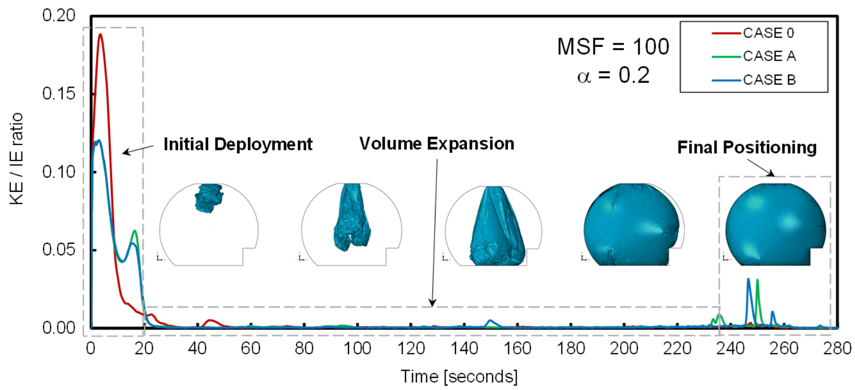

(a)

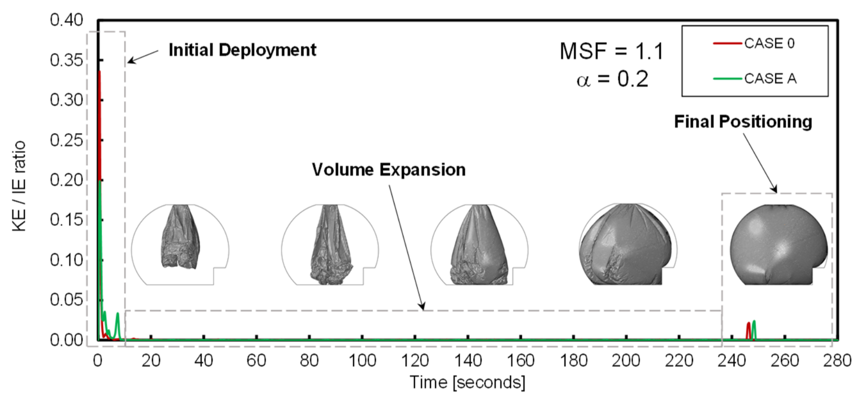

(b)

Figure 26. Time history of kinetic (KE) to internal (IE) energy ratio for: (a) MSF = 100, α = 0.2, Cases 0, A and B; (b) MSF = 1.1 and α = 0.2, Cases 0 and A.

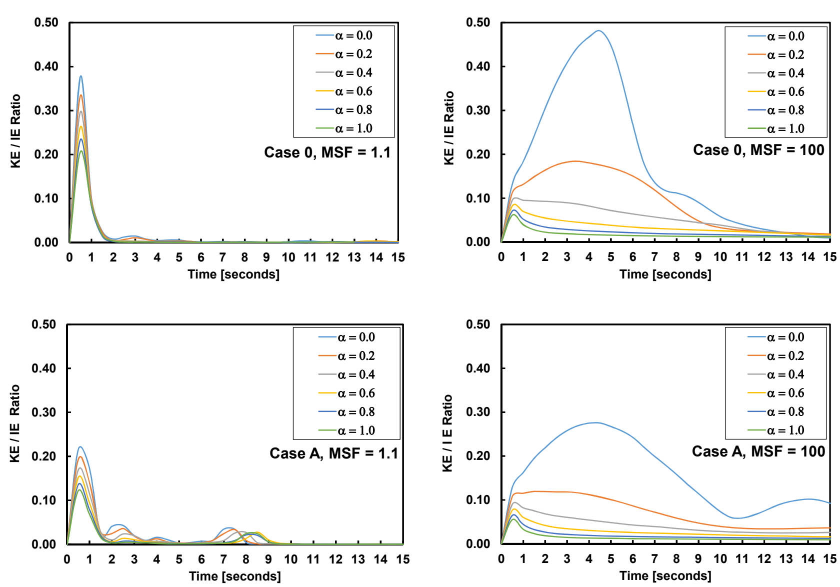

Figure 27. Kinetic (KE) to internal (IE) energy ratios for initial deployment for different values of mass-proportional damping and two values of MSFs. Case 0 (top) and Case A (bottom).

Figure 28. Sequence of Initial deployment (t = 0 to t = 15 sec) for Case 0 as function of MSF and select mass-proportional damping factors. Air mass flow rate $\dot{m}$ = 0.48 kg/sec.

Figure 29. Sequence of Initial deployment ($t = 0$ to $t = 15$ sec) for Case A as function of MSF and select mass-proportional damping factors. Air mass flow rate $\dot{m} = 0.48$ kg/sec.

TABLES

Table 1. Summary of mesh convergence study.

	Number of Elements	Average Element Size	Computing time	Average Hoop Stress in Cylindrical Region	
	[#]	[m]	[hours]	S_{11} [Pa]	% Error
Analytical value σ_1				$24.71 \cdot 10^6$	
Mesh A	27528	0.07	0.52	$24.70 \cdot 10^6$	0.05
Mesh B	48948	0.06	1.30	$24.68 \cdot 10^6$	0.13
Mesh C	95902	0.05	3.42	$24.70 \cdot 10^6$	0.06

Table 2. Effect of Mass Scaling Factor (MSF) on unconfined inflation.

MSF	Total Computation Time [hours]	Peak KE /IE ratio
1	456	0.0008
10	83	0.0075
100	46	0.0736
1000	19	0.2896

Table 3. Thermodynamic properties of Air [20].

Universal Gas Constant	8314.3	$J\,/\,(kmol \cdot °K)$
Molecular Weight	28.97	$kg/kmol$
Absolute Zero Temperature	0.0	K
Ambient Temperature	288.15	K
Ambient Temperature	15	°C
Ambient Pressure at sea level	101315.0	Pa
Density of Air	1.225	kg/m^3
Heat Capacity Ratio γ (gamma)	1.4	

Table 4. Coefficients of Shomate equation for air [21].

a	28110	$J/kmol \cdot K$
b	1.967	$J/kmol \cdot K^2$
c	0.004802	$J/kmol \cdot K^3$
d	-0.000001966	$J/kmol \cdot K^4$
e	0.0	$JK/kmol$

Table 5. Percentages of improvement in the contact area (CAREA).

Case	Contact Area [m^2]	% of Increase	Improvement due to:
NC	57.7	-	Nominal Contact area
0	60.8	5.4	Confining effect
A	66.8	15.8	Confining effect + release of membrane
B	67.3	16.6	Confining effect + release of membrane